

TESS observations of non-Be fast rotators

Yaël Nazé^{1,*}, Nikolay Britavskiy^{1,2}, and Jonathan Labadie-Bartz³

¹ Groupe d'Astrophysique des Hautes Energies, STAR, Université de Liège, Quartier Agora (B5c, Institut d'Astrophysique et de Géophysique), Allée du 6 Août 19c, B-4000 Sart Tilman, Liège, Belgium
e-mail: ynaze@uliege.be

² Royal Observatory of Belgium, Avenue Circulaire/Ringlaan 3, 1180 Brussels, Belgium

³ LESIA, Paris Observatory, PSL University, CNRS, Sorbonne University, Université Paris Cité, 5 place Jules Janssen, 92195 Meudon, France

July 12, 2024

ABSTRACT

Aims. The variability of fast-rotating Oe/Be stars has been reported in detail in recent years. However, much less known about the behaviour of fast-rotating OB stars without known decretion disks, and hence it is difficult to identify the commonalities and differences in the photometric variability of these two populations, especially with regards to their pulsational properties and their link with the presence of circumstellar material.

Methods. Via an in-depth literature search, we identified a set of fast-rotating ($v \sin(i) > 200 \text{ km s}^{-1}$) early B-type stars not known to have disks. TESS and *Kepler* light curves were built for 58 stars that appear isolated (no bright neighbour within $1'$ and no known companion) to avoid contamination of the light curves. Frequency spectra were calculated and then analysed to determine the noise level and the presence of significant signals above the noise.

Results. Red noise is detected in all targets, without obvious correlations between noise and stellar parameters. Long-term changes are much less frequent than in Be stars, with only 12% of our targets having the variability below 0.5 d^{-1} dominating their frequency spectrum. In contrast, strong frequency groups are detected in about a third of targets, as in Be stars. These groups generally occur in pairs with harmonic frequencies, as is usually seen in Be stars, but with the first group more often displaying larger amplitudes. Finally, the most frequent variability is due to isolated frequencies in the $0.5\text{--}6 \text{ d}^{-1}$ range (which is found in two-thirds of cases and dominates the spectra in 42% of the sample). Higher-frequency signals (up to 40 d^{-1}) are sometimes also detected but rarely (only 12% of stars) appear as the strongest ones of the frequency spectra. Overall, fast-rotating B-type stars, with or without disks, display similar photometric properties, except as regards their longer-term behaviour.

Key words. Stars: early-type – Stars: rotation – Stars: oscillations

1. Introduction

For more than a century, a subgroup of massive OB stars were found to display, at least from time to time, Balmer emission lines in their spectra. This led to the creation of the “classical Oe/Be stars” category. These stars are now understood to be surrounded by a decretion disk, which is responsible for the remarkable emissions (for a review, see Rivinius et al. 2013). Another particularity shared by objects in this category is fast rotation (see Frémat et al. 2005 and, for an in-depth review, see Zorec 2023). Combined with the detection of low-mass hot companions (e.g. Wang et al. 2021) or of a truncation of disks (Klement et al. 2019), this suggests that Be stars actually are, at least sometimes, binary interaction products, in line with theoretical proposals (van Bever & Vanbeveren 1997; Shao & Li 2014). The initially more massive star of the system has lost mass which was at least partially accreted by the companion. Angular momentum was also transferred during the event, speeding up the accreting companion while increasing its mass and it eventually became an Oe/Be star.

When monitored, such stars display changes on various timescales. First, there are ejections of the material building the disk, which then clears from the inside out. This should

correspond to brightenings or dimmings, depending on geometry (see the numerous observational and theoretical studies, e.g. Hubert & Floquet 1998; Keller et al. 2002; Mennickent et al. 2002; Sigut & Patel 2013; Ghoreyshi et al. 2021 and references therein), followed by a return to the baseline occurring on days, weeks, or months. Second, there are non-radial pulsations, often at low frequencies ($<5 \text{ d}^{-1}$, Cuypers et al. 1989) and/or rotational signals (Balona & Ozuyar 2021). Finally, there is also stochastic red noise, as usual in massive stars (Nazé et al. 2020; Labadie-Bartz et al. 2022).

In recent years, the advent of space facilities, such as *CoRoT* (Convection, Rotation and planetary Transits), *Kepler*, or TESS (Transiting Exoplanet Survey Satellite), as well as long-term campaigns by ground observatories (e.g. *KELT*), has enabled astronomers to examine the variability of Oe/Be stars in detail (Gutiérrez-Soto et al. 2007; Labadie-Bartz et al. 2017; Semaan et al. 2018; Balona & Ozuyar 2020; Nazé et al. 2020; Labadie-Bartz et al. 2022). Statistics were established on the occurrence rates of the different variation types, and their typical characteristics were derived. However, the impact of the presence of disk circumstellar material on this variability on timescales of a few days and shorter has not yet been fully clarified.

* F.R.S.-FNRS Senior Research Associate

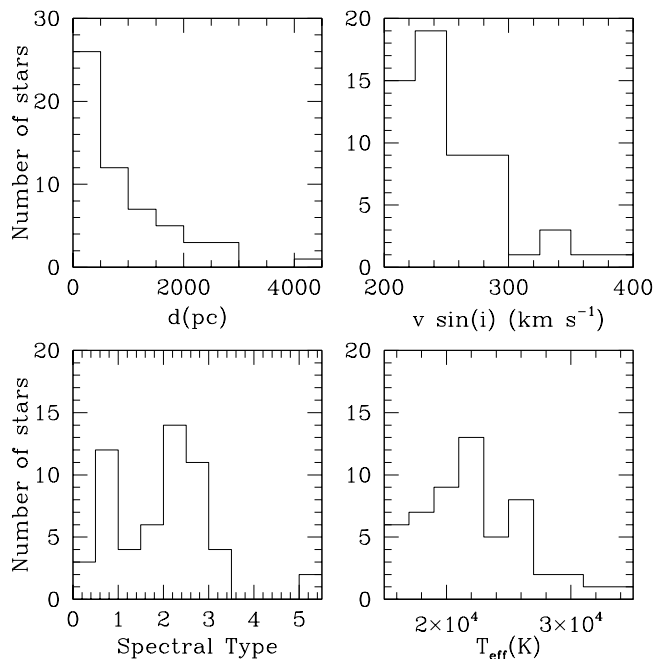


Fig. 1. Histograms of the distances, projected rotational velocities, spectral types, and temperatures of our targets.

In this study, we decided to use high-cadence photometric data from the space telescopes *TESS* and *Kepler* to offer a counterpoint to the Be star studies. Observational studies of non-Be fast-rotating massive stars also suggest that such stars arise from binary interactions (e.g. O stars in Britavskiy et al. 2023), which would mean that they share a common origin with Oe/Be stars. However, if they do not belong to the Oe/Be category, then circumstellar material is absent. The comparison of the two samples - fast-rotating Be and non-Be stars (sometimes called ‘Bn’ stars) - would then clarify the impact of disks on the recorded variability, and/or any intrinsic differences in photospheric signals. The study of non-Be stars could also help us understand the origin of stellar rotation. Overall, fast rotation can be primordial or arise from a post-mass transfer spin-up or even a merger event. Any difference in the observed variability could be linked to differences in the inner layers. It is therefore important to have a significant sample of well-studied targets from both Be and non-Be domains in order to systematise their properties and draw a global picture. The paper is divided as follows: Sect. 2 presents the sample and the datasets, while Sect. 3 focuses on red noise and Sect. 4 on the other variabilities. A conclusion then summarises the results.

2. Observing fast rotators

2.1. Defining the sample

While several studies have investigated the rotation of massive stars, often for a specific cluster, a single overall catalogue of precise projected rotational velocities of stars remains difficult to find. Therefore, we decided to build our own sample. To this aim, we performed an in-depth search of the literature in several steps. First, the VizieR database¹ was explored to identify catalogues dedicated to rotation rates. This led to the identification of a large series of papers

(Abt et al. 2002; Bragança et al. 2012; Cochetti et al. 2020; Daflon et al. 2007; David & Hillenbrand 2015; Garmy et al. 2015; Głębocki & Gnaniński 2005; Hanes et al. 2018; Howarth et al. 1997; Huang & Gies 2006a; Huang et al. 2010; Levenhagen & Leister 2006; Marsh Boyer et al. 2012; Penny & Gies 2009; Simón-Díaz & Herrero 2014; Strom et al. 2005; van Belle 2012; Wolff et al. 2007; Xiang et al. 2022). Their associated tables were then filtered to keep only stars with fast rotation, defined as $v \sin(i) > 200 \text{ km s}^{-1}$. This choice of threshold was done because, above it, most objects should have been spun up by binary interactions (de Mink et al. 2013). In addition, we kept only the hottest B-type main sequence stars, that is those with spectral types between B0V and B3V (with luminosity class IV also allowed, but not supergiants as such evolved stars do not display Be features) or with effective temperatures T_{eff} in 17000–31500 K and $\log(g) > 3.7$ (the chosen criterion depends on the catalogue as some catalogues uses spectral types, while others rely on temperature and gravity).

Second, we eliminated from this list known Be stars (either listed as such in SIMBAD² or belonging to the BeSS catalogue³) as we wish to investigate fast rotators but *without* disks. We also discarded obvious binaries (“SIMBAD categories EB*, SB*, and El*”), magnetic stars, and young objects (“SIMBAD category YSO*”) to avoid contamination by unrelated objects. Finally, to be certain to get a light curve from the fast-rotating object despite the rather coarse spatial resolution of *TESS*, we also took out stars possessing any nearby bright companions in the *GAIA* Data Release 3 catalogue (a companion within 1’ of the star and with $\Delta(G) < 2.5 \text{ mag}$).

As a last step, literature was examined in detail for each object of this cleaned list. This allowed us to discard further binaries as well as objects whose stellar parameters in recent studies lie outside of our selection criteria. We note that a few objects listed as B5 but with temperatures in our allowed temperature range were kept, as were a few cases of slightly too hot or too cold stars listed with allowed spectral types. Our final list comprises 61 objects, among which are several well-known pulsators. Five of them were not observed by *TESS*, but two of these five have *Kepler* (K2) light curves. Our sample therefore comprises 58 stars in total (see Table A.1 for details).

Distribution of distances (from Bailer-Jones et al. 2021), projected rotational velocities, spectral types, and temperatures are provided in Figure 1. These histograms show that two-thirds of the targets lie closer than 1 kpc, and 90% of them display projected rotational velocities between 200 and 300 km s^{-1} . Targets are also nearly evenly distributed between spectral types B0–1.5 and B2–3.

Using *STILISM*⁴ (Lallement et al. 2014), we calculated the reddenings based on the SIMBAD galactic coordinates and the known distances. Bolometric luminosities were then obtained in the usual way using the observed *V* magnitudes (from Simbad), the derived reddenings (assuming $R_V = 3.1$), the known distances, and bolometric corrections BC_V calculated from the effective temperatures using the formula of Pedersen et al. (2020). In four cases, temperatures were not known; hence, typical temperatures and bolometric corrections for the targets’ spectral types were taken from Pecaut & Mamajek (2013)⁵. In four other

² <http://simbad.u-strasbg.fr/simbad/>

³ <http://basebe.obspm.fr/basebe/> and (Neiner et al. 2011), from Fall 2022

⁴ <https://stilism.obspm.fr/>

⁵ see http://www.pas.rochester.edu/~emamajek/EEM_dwarf_UBVJHK_colors_Teff.txt

¹ <https://vizier.cds.unistra.fr/>

cases, there is no V magnitude in SIMBAD, no distance in Bailer-Jones et al. (2021), or no reddenings (distances are larger than the maximum distance allowed by `STILISM`) hence typical bolometric luminosities for the targets' spectral types were used. These cases are identified by m in Table A.1. To conclude on this subject, one remark must be made. Most of our targets were rarely studied and their parameters often come from global studies, not papers dedicated to one specific target. The stellar parameters may thus suffer from some uncertainties, especially since their derivation is quite delicate for fast-rotating stars (see e.g. Frémat et al. 2005). As a check, we compared the derived bolometric luminosities to those expected in Mamajek's calibration for the targets' spectral types (or temperatures, for the two B5 cases and the two cases without known spectral types): two-thirds of the targets had these luminosities agreeing within a factor of two (or 0.3 dex, i.e. about half a subtype) and only 13% had them differing by more than a factor of four (or 0.6 dex). As a second check, we compared the targets' temperatures to the expected temperatures for their spectral types: the difference was less than 2 kK for 52% of stars and more than 5 kK for only 15% of them. For CPD-50 9216 and CPD-48 8710, the observed mismatches could be easily solved as their temperatures and derived luminosities appear fully compatible with a B2 spectral type: this suggests a (small) misclassification in their cases. Overall, larger differences are found for more distant (> 1 kpc) targets. This is unsurprising as distant objects are certainly amongst the least studied objects of our sample. Nevertheless, considering the difficulty to secure parameters of fast rotators, the large fraction of good agreements may be underlined.

As a last step, we estimated $v \sin(i)/V_c$. In view of the uncertainties in the stellar parameters (see above), no attempt was made to correct for inclination. For the same reason, we cannot securely match the targets to the closest evolutionary tracks to derive ages or critical velocities. A crude estimate was then calculated from $V_c = \sqrt{GM_*/R_*}$ with the stellar radius evaluated from $L_{\text{BOL}} = 4\pi R_*^2 \sigma T_{\text{eff}}^4$ and the stellar masses M_* the typical ones for the considered spectral types in Mamajek's calibration. Table A.1 provides the $v \sin(i)/V_c$ (see Section 4 for further details), except for two targets without spectral types and two others with a (most probably incorrect) B5V type. Our targets lie mostly between ratios of 0.3 and 0.6. No target is detected with a very low ratio but this is a known observational bias: while fast-rotating Be stars can be recognised at nearly all inclinations as their detection is based on the presence of $H\alpha$ emission, fast-rotating B-stars that are not surrounded by circumstellar material can only be recognised from their broad lines, in other words if they are not seen too close to pole-on. In the Bn sample of Cochetti et al. (2020), which is mostly composed of stars with later spectral types, the lowest $v \sin(i)/V_c$ ratios were around 0.4, the highest ones near 1.0, and the average around 0.6: their stars thus display, on average, somewhat higher ratios than stars in our sample. The ratios observed for our stars also peak at slightly lower values than for the Be sample of Cochetti et al. (2020). We also calculated critical velocities from *GAIA* masses and radii (Kervella et al. 2022). This resulted in an average increase in the $v \sin(i)/V_c$ ratios of 50%, with most values in 0.5–0.7 and a few ratios now larger than 1. However, such *GAIA* parameters are known to be quite uncertain for the hottest stars. In the literature, critical velocities have been published for three stars (HD 5882, HD 35532, and HD 87015; see Huang et al. 2010) and these values are 30% lower than our first estimates for these stars and 10% than the second ones. Overall, our first estimates may thus be biased towards slightly too low ratios (and the second estimates towards too large ones). Nevertheless, we kept these first

estimates for the moment, to be conservative (and avoid biasing towards too large values) while awaiting for future, better determinations from detailed spectroscopic analyses.

2.2. Light curves

Launched in April 2018, the TESS satellite (Ricker et al. 2015) provides photometric measurements for nearly all of the celestial sphere. Observations are organised by “sectors” with durations of about 25 d, and this paper uses data up to Sector 74. All but one of our TESS targets have been observed in several Sectors (generally 2–5, but up to 19); these light curves were examined independently. In each sector, preselected stars are measured every 2 min, while usual sky images are taken with a cadence of 30 min up to Sector 26, 10 min for Sectors 27–55, and 200 s afterwards. The sector duration leads to a natural peak width in frequency space of $1/25$ d, i.e. 0.04 d^{-1} , while the observing cadences of 30 min, 10 min, 200 s, and 2 min lead to Nyquist frequencies of 24, 72, 216, and 360 d^{-1} , respectively. The main steps of data reduction (pixel-level calibration, background subtraction, flat-fielding, and bias subtraction) are done by a pipeline similar to that designed for the *Kepler* mission.

For 2 min cadence data, simple aperture photometry (SAP) as well as time series corrected for crowding, the limited size of the aperture, and instrumental systematics (Pre-search Data Conditioning SAP flux - PDC) were downloaded from the Mikulski Archive for Space Telescopes (MAST)⁶. We kept only the best quality (quality flag=0) data. In each case, we compared the SAP and PDC light curves. Generally, both curves were similar or PDC light curves were better. Only in a few cases were SAP light curves preferred as PDC photometry appeared noisier.

For the data with other cadences, individual light curves were extracted for each target from TESS full frame images. Aperture photometry was done on image cutouts of 50×50 pixels using the Python package `Lightkurve`⁷. A source mask was defined from pixels above a given flux threshold (generally 10 Median Absolute Deviation over the median flux, but it was decreased for faint sources or increased if neighbours existed). The background mask was defined by pixels with fluxes below the median flux (i.e. below the null threshold), thereby avoiding nearby field sources. To estimate the background, two methods were used: first, a principal component analysis, usually with five components; second, a simple median. In each case, the two background-subtracted light curves were compared. Generally, principal-component-analysis-corrected light curves were better but in a few cases they appeared noisier hence the curves using the median correction were preferred.

The two targets observed with *Kepler* (HD 138485 and HD 142378) are bright and have saturated the detector. In such cases, the star spot is larger due to spilled charges. For the latter star, the pipeline-selected aperture was sufficiently large to capture most light hence the pipeline light curve is usable⁸. This was not the case for the former star, leading to weird results with erratic photometry. Fortunately, Pope et al. (2019) produced light curves for several saturated stars in the framework of the HALO survey⁹, among which HD 138485 (EPIC 200194914). In both cases, as for the 2 min cadence data, only the best quality data were considered and the corrected curves were favoured over

⁶ <https://mast.stsci.edu/portal/Mashup/Clients/Mast/Portal.html>

⁷ <https://docs.lightkurve.org/>

⁸ With identifier `ktwo205104403-c02_llc`, it can be downloaded from MAST.

⁹ <https://archive.stsci.edu/hlsp/halo>

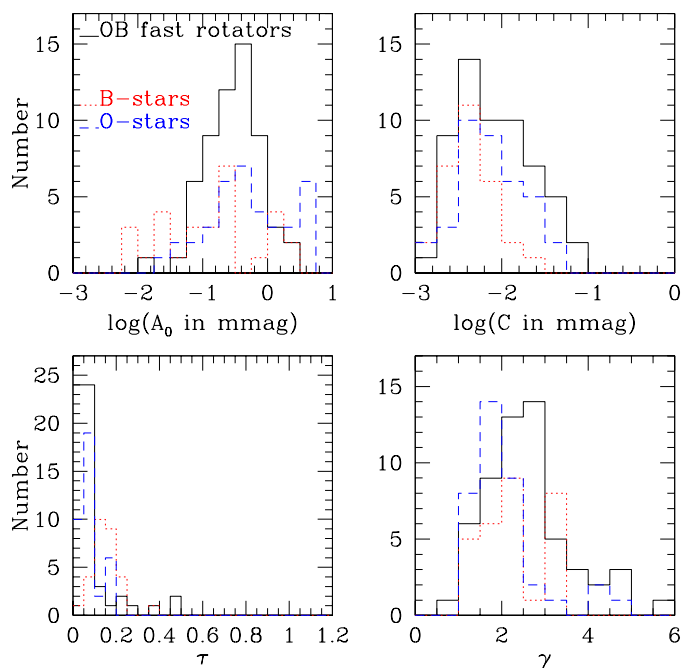


Fig. 2. Histograms of red noise parameters for our fast rotators (solid black line), compared to those determined for O and B-type stars by Bowman et al. (2020, - dotted blue and red lines, respectively).

the SAP data. The two targets were observed every 30 min for about 80 d with *Kepler*, leading to a Nyquist frequency of 24 d^{-1} and a natural peak width of 0.01 d^{-1} .

For all 221 light curves, the raw fluxes were converted into magnitudes using the usual formula $mag = -2.5 \times \log(flux)$ and the mean was then subtracted. For the TESS data with cadences larger than 2 min, data points with errors larger than the mean of the errors plus three times their 1σ dispersion were also discarded. In addition, a few isolated outliers and a few short temporal windows with sudden high scatter were eliminated from the few affected light curves. For seven targets, a trend was detected in one sector but not others, suggesting an instrumental effect: the linear or parabolic best-fit of the trend was thus calculated and taken out. Finally, the frequency spectrum of each light curve was calculated using a modified Fourier algorithm taking into account the presence of gaps (Heck et al. 1985; Gosset et al. 2001; Zechmeister & Kürster 2009). The frequency resolution was set to one tenth of the natural peak width¹⁰. Figures showing all light curves and their associated frequency spectra are available on Zenodo¹¹.

3. Red noise

With the advent of space-based high-cadence photometry, it became clear that massive stars (with types O, B, WR, or LBV) generally display a gradual increase in power towards low frequencies, i.e. a so-called ‘red noise’ (Blomme et al. 2011; Rauw et al. 2019; Bowman et al. 2019; Nazé et al. 2021). Our sample is no exception: all targets display red noise. Several origins have been proposed to explain this ubiquitous variability, most notably a combination of internal gravity waves excited at

the interface between the convective core and the radiative envelope (Rogers et al. 2013) or in a subsurface convection zone (Blomme et al. 2011).

Characterising the properties of this noise is important for two reasons. First, its characteristics should be linked to the physical processes giving rise to it; hence, they could help us better understand its origin. Second, white+red noise represents a varying background to be taken into account while assessing the significance of any other signal and hence needs to be known. The variation with frequency of the white+red noise is usually fitted using the generalised formalism of a suggestion by Harvey (1985):

$$A(\nu) = C + \frac{A_0}{1 + (2\pi\tau\nu)^\gamma} \quad (1)$$

where $A(\nu)$ is the amplitude of the frequency spectrum at frequency ν ¹², A_0 is the red noise level at null frequency, τ the mean lifetime of the structures producing the red noise, γ the slope of the linear decrease, and C the white noise level. Before the fitting, done through a Levenberg-Marquardt algorithm, the larger peaks of the frequency spectra were excised using a simple amplitude threshold to avoid biasing the red noise background estimate.

As there is no formal error on frequency spectrum amplitudes, the errors on the red noise parameters are difficult to formally calculate. As a first approximation, we followed the procedure outlined in Nazé et al. (2021): parameter errors were assumed to be equal to the square root of the diagonal elements of the best-fit variance-covariance matrix, multiplied by the square root of $\chi^2(\text{best fit}) / (0.5 \times N_{\text{data}} - 4)$. This assumes that the best-fit reduced χ^2 should amount to one and that the actual number of independent frequencies is half the number of data points in the light curve.

Appendix B provides the best-fit noise parameters for the 221 frequency spectra. It should be noted that the white noise level is usually reached only at very high frequencies, that is frequencies usually much larger than the Nyquist frequency of 24 d^{-1} of the lowest cadence data (identified by *Kepler* and TESS Sectors 1–26 without asterisk in Col. 2 of Tables A.1 and B.1 in Appendix). Therefore, the parameters associated with these lower cadence light curves must be taken with caution, whereas those taken with the two highest cadence (i.e. TESS Sectors >55 or sectors with an asterisk in the tables). We note also that the errors may still be somewhat underestimated, as similar light curves may have parameters varying by more than their 1σ errors.

To perform comparisons, a single set of parameters should be used for each star. We therefore choose the values associated with the light curve with the highest cadence. If several such curves are available for a given target, the values from the most recent observation are usually chosen (parameters generally appear similar except in a few cases for which that best-fit curve visually seems obviously less suitable than that of another sector). The parameters’ distribution is compared to that of other massive stars in Fig. 2. As can be seen, the parameter values found for our fast rotators are in excellent agreement with the ranges found for a set of 37 O stars and 29 early B-type stars by

¹⁰ We also consider this value as representative of the frequency uncertainty, although some authors are even more conservative (e.g. Kallinger et al. 2008 favours a value of one fourth of the peak width).

¹¹ <https://zenodo.org/doi/10.5281/zenodo.12699682>

¹² Formally, stochastic processes such as white and red noises sum up quadratically and not linearly; hence, power should be fitted by this formula rather than amplitude. Custom in the massive star field however favours using the latter, which we followed. We note that the results, such as the detection of physical trends, are not affected by this choice (see Nazé et al. 2021 for a detailed comparison).

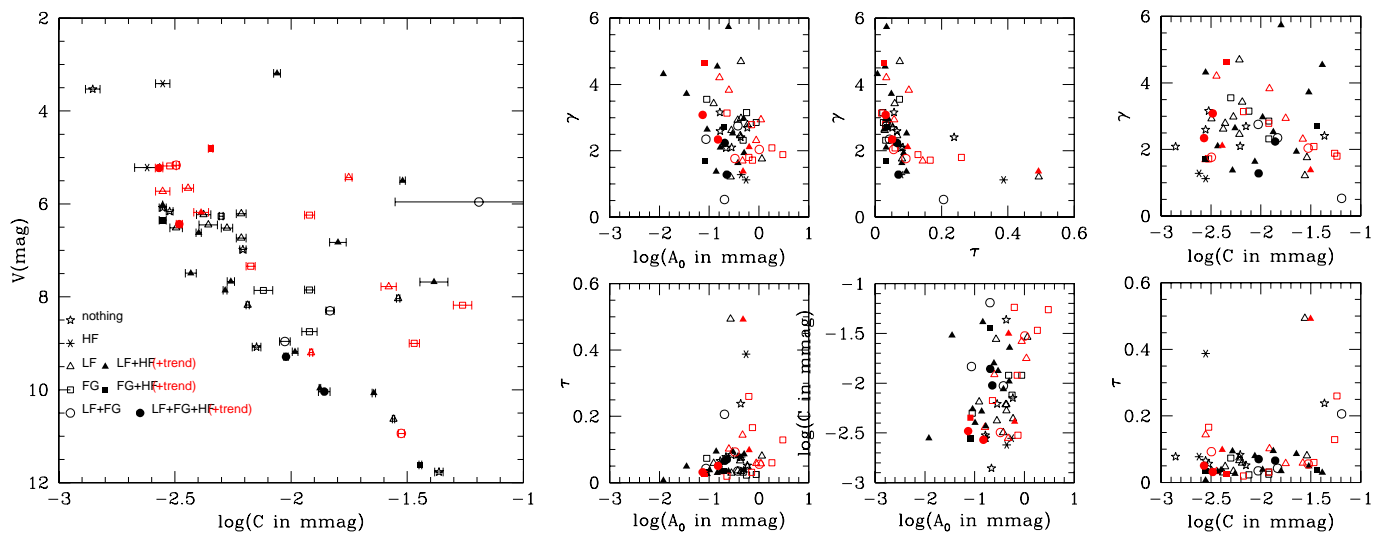


Fig. 3. Comparison between red noise parameters. *Left:* Comparison between the white noise level, C , and the V magnitude of all targets. Symbols indicate the type of recorded variability (see Sect. 4): objects without any variability beyond red noise are shown as stars, objects with only high-frequency (HF) signals as asterisks, objects with dominating low-frequency (LF) signals as triangles, objects with strong frequency groups (FG) as squares, and objects with both LF and FG signals as circles. For the last three categories, the symbols are filled if high-frequency signals also exist, and empty otherwise. If trends or very low-frequency signals are detected, the symbols are shown in red. *Right:* Two-by-two comparison between red noise parameters, using the same symbols.

Bowman et al. (2020). Fast rotation thus does not affect much the physical processes responsible for these noises.

We compare the white noise levels C to the targets’ magnitudes in Fig. 3. As was found for evolved massive stars (Nazé et al. 2021), the range of white noise levels appears restricted for the faintest stars; in other words, lower C values can only be found for the visually brighter objects. This could be expected as it simply reflects a larger impact of photon noise on the recorded light curves from faint stars: for them, a low intrinsic noise level may remain hidden. As this instrumental effect is not frequency-dependent, it does not affect much the red noise level A_0 . In this context, it could be noted that the red noise level always appears larger than the white noise level, with an average ratio of ~ 50 (Fig. 2).

To search for correlations between noise parameters, we calculated the Pearson coefficients (see also Fig. 3) but none indicated a strong correlation ($> 90\%$) – the largest value, 44%, was found for the $A_0 - C$ relationship. Strong correlations with projected rotational velocity, effective temperature, or bolometric luminosities were also not obvious – the largest value is only 44%, and it was found for $\log(A_0) - \log(L_{\text{BOL}})$ pairs. Finally, stars were plotted in the Hertzsprung-Russell diagram, with symbols coloured as a function of red noise parameters. While Bowman et al. (2020) found that the red noise amplitude A_0 and the lifetime $\tau = 1/(2\pi\nu_{\text{char}})$ decreased towards the zero-age main sequence (ZAMS; i.e. higher temperatures and lower luminosities), we find no such correlation here (Fig. 4). However, the stellar parameters of our targets may be less precisely constrained as they often are less studied objects (see Section 2). Our conclusion could therefore benefit from a confirmation after an in-depth spectroscopic investigation of all targets, taking into account the impact of their fast rotation, become available.

4. Other variations

Figure 5 displays examples of frequency spectra, showing the main features that are discussed in this paper: red noise, long-

term variations, frequency groups (FGs), and isolated peaks. Signals are considered significant if their amplitude is five times larger than the best-fit red+white noise model computed at that frequency (i.e. $S/N = 5$, as recommended by Baran et al. 2015). For TESS, if data from several sectors are available, it may happen that a signal appears at the same frequency in all sectors but is formally significant in only a subset of them: such signals were also added to the list of detected features. It may be noted that only 6 targets (HD75869, HD75869, HD125238, HD166197, HD193794, and LS III +57 89, or 10% of the sample) do not show any significant variability beyond white+red noise.

4.1. Long-term variations ($f < 0.5 \text{ d}^{-1}$)

As in Labadie-Bartz et al. (2022), we defined long-term variations as signals detected with $> 2 \text{ d}$ timescales. However, the duration of the *Kepler* observations and the duration of one TESS sector are limited, hence very slow variations (with timescales $> 30 \text{ d}$) cannot be easily identified. We thus focused on long-term variations occurring on timescales of a few days to a few weeks.

In Be stars, ‘flickers’ are often detected (in about one-third of early-type stars observed in the first year of the TESS mission, see Labadie-Bartz et al. 2022). They are characterised by their shape, with a change in brightness (increase or decrease) followed by a return to the baseline luminosity; they are not oscillations around an average luminosity. In our sample, the only variations that could maybe be related to such variability are found in HD68217 and CPD-50 9216 (so an incidence rate of maximum 2/58). Flickers are thus extremely rare amongst fast-rotating, non-Be stars. This might be understood as such variability is thought to be related to disk-building events but our stars do not display disks while Be stars do.

Two other types of long-term variability are low-frequency FGs and isolated low-frequency peaks. We defined isolated peaks as peaks in the frequency spectrum that are clearly dominating their neighbourhood, that is, at least twice larger than

Table 1. Properties of strong FGs detected in our sample.

Name	$f(G_1)$ in d^{-1} (amplitude)	$f(G_2)$ in d^{-1} (amplitude)	$f(G_{>2})$ in d^{-1} (amplitude)
NGC 869 133	2.65 (2.7–3.2 mmag)	5.34 (1.1–1.5 mmag)	
BD+62 657	0.96 (1.1–1.5 mmag)		
HD34748	2.24 (0.6–0.7 mmag)	4.19 (0.3–0.5 mmag)	8.50 (0.2–0.3 mmag)
HD249845	1.76 (6.8–11.8 mmag)	3.45 (4.2–8.8 mmag)	
HD254042	1.51 (2.4–3.3 mmag)	very low amplitude	
HD259865	1.39 (2.0–2.4 mmag)	2.66 (1 mmag)	G_3 very faint
HD46994	1.70 (4 mmag)	3.90 (9.0–13.5 mmag)	8.10 (1.5 mmag)
HD47360	1.68 (8.1–10.5 mmag)		
HD52463	1.71 (0.4–1.0 mmag)	4.04 (0.7–1.4 mmag)	5.65 (0.3–0.4 mmag) ^a , 7.36 (0.2–0.3 mmag) ^a , 11.4 (0.2 mmag) ^a
HD56876	4.31 (0.7 mmag)		
HD67536	1.79 (8.9–13.5 mmag)	3.60 (3.6–7.4 mmag)	
HD68217	1.93 (1.3–2.7 mmag)		
HD68962	2.34 (1.5–2.0 mmag)	4.77 (5.5–7.0 mmag)	9.40 (0.5–1 mmag), 14.2 (0.5–0.9 mmag), 23.5 (0.06–0.18 mmag), 28.1 (0.07–0.08 mmag), 33.0 (0.05–0.06 mmag)
HD81347	0.76 (1.3–1.6 mmag)	1.55 (0.8–1.0 mmag)	2.31 (0.1–0.3 mmag), 4.55 (0.07 mmag)
HD93501	0.96 (4.5–9.5 mmag)	1.86 (3.2–9.7 mmag)	
HD108257	2.92 (0.9–1.0 mmag)	4.80 (2.7–3.0 mmag)	6.71 (0.1–0.2 mmag), 9.60 (0.1 mmag), 14.3 (0.2 mmag)
HD142378	1.89 (1.6 mmag)		
CPD-50 9216	1.37 (4.8–7.4 mmag)	2.69 (3.1 mmag)	
HD168905	1.88 (1.1–1.4 mmag)	3.89 (0.3–0.4 mmag)	
HD216092	3.10 (2.1–3.2 mmag)	6.05 (1.2–2.4 mmag)	
NGC 7654 485	1.96 (0.6–1.0 mmag)		
HD223145	1.39 (1.1–1.4 mmag)	2.77 (0.2–0.3 mmag) ^b	3.94 (0.1 mmag) ^b

Notes. Label ^a indicates information valid for Sectors 6 and 7 only, ^b for Sectors 1 and 2 only. Due to the variable nature of these FGs, frequencies and amplitudes should be considered approximate.

the next highest peak in the vicinity. Eight targets showed such isolated low-frequency peaks, with one more star showing such signals in one sector. These are:

- HD47360: $f=0.140 d^{-1}$ (amplitude of 43–51 mmag)
- HD56876: $f=0.424 d^{-1}$ (amplitude of 0.7 mmag)
- HD87152: $f=0.264 d^{-1}$ (amplitude of 4.4–5.8 mmag)
- HD97499: $f=0.376 d^{-1}$ (amplitude of 1.5–1.8 mmag)
- HD150745: $f=0.416 d^{-1}$ (amplitude of 1.6–3.4 mmag)
- HD168905: $f=0.352 d^{-1}$ (amplitude of 0.6 mmag) and $0.486 d^{-1}$ (amplitude of 0.7–0.8 mmag)
- HD180968: $f=0.174 d^{-1}$ (amplitude of 4.4–7.3 mmag)
- CI* Berkeley 86 HG 261: $f=0.174 d^{-1}$ (amplitude of 2.0–2.7 mmag)
- HD46883 in Sector 33: $f=0.432 d^{-1}$ (amplitude of 5.2 mmag), with its close harmonics $0.876 d^{-1}$ (amplitude of 5.7 mmag)

A range in amplitudes is provided when the amplitude is seen to change from sector to sector.

In contrast, a FG is a collection of many closely spaced peaks with several showing similar amplitudes. In Be stars, such groups most often appear at frequencies of 0.5–6. d^{-1} , but they may be complemented by a similar group at even lower frequencies (called ‘ G_0 ’ in Labadie-Bartz et al. 2022). This is also the case here: G_0 groups are not found alone. Four cases were spotted amongst our targets. It must be noted that, as low frequencies are always affected by red noise, it may become difficult to distinguish a low-amplitude FG from strong red noise. In five additional cases, the G_0 groups should thus be considered as tentative (hence the question marks in the list below). In the following list, the frequencies and amplitudes are those of the highest peak of the group, usually close to group centre. As such FGs are quite variable from one sector to the next, they are much less well defined than strong isolated peaks, of course, so that values are approximate. Cases are:

- HD67536: $G_0 \sim 0.25 d^{-1}$ (max. amplitude of 4.1–15.0 mmag)
- HD68962: $G_0 \sim 0.1 - 0.2 d^{-1}$ (max. amplitude of 1 mmag)
- HD93501: $G_0 \sim 0.19 d^{-1}$ (max. amplitude of 6.7–12.0 mmag)

- CPD-50 9216: $G_0 \sim 0.17 d^{-1}$ (max. amplitude of 6.7–10.8 mmag)
- HD68217: $G_0 \sim 0.16 d^{-1}$ (max. amplitude of 6.3–12.4 mmag)?
- HD87015: $G_0 \sim 0.39$ or $0.57 d^{-1}$ (max. amplitude of 1.0–1.4 mmag)?
- HD108257: $G_0 \sim 0.61 d^{-1}$ (max. amplitude of 0.4–0.5 mmag)?
- NGC 7654 485: several peaks below $0.5 d^{-1}$, an ill-defined G_0 ?
- HD223145: $G_0 \sim 0.34 d^{-1}$ (max. amplitude of 1.6–2.3 mmag)?

In total, there are thus 12 cases with clear low-frequency variability, plus 6 good candidates. However, this low-frequency variability clearly dominates the frequency spectrum (i.e. has a larger amplitude than any other signal) in only seven cases: HD46883 (Sect. 33), HD47360, HD87152, CPD-50 9216, HD150745, CI* Berkeley 86 HG 261, and HD223145. This represents a 12% incidence rate, while Labadie-Bartz et al. (2022) counts 51% of ‘longer-term trends dominating’ cases in their TESS sample of early Be stars and Labadie-Bartz et al. (2017) noted that about half of their early Be sample observed with *KELT* displays long-term variability or periodicities of 2–200 d^{-1} . Definitely, be it for flickers or other variabilities, the fast-rotating stars without (known) disks appear much less variable on long timescales. Disk built-up and disappearance most probably explain this difference.

As a final note on long-term changes, we can also compare the frequency spectra of the same targets taken at different times (i.e. in different sectors). Compared to what is seen in Be stars (Labadie-Bartz et al. 2022), the spectra of our targets appear overall more stable, or rarely with radical changes in appearance. One exception is HD46883 which appears much more variable (stronger signals at low frequencies) in Sector 33 compared to Sector 6. More precisely, the star displays a larger variability for a few cycles around Julian date 2 459 208.

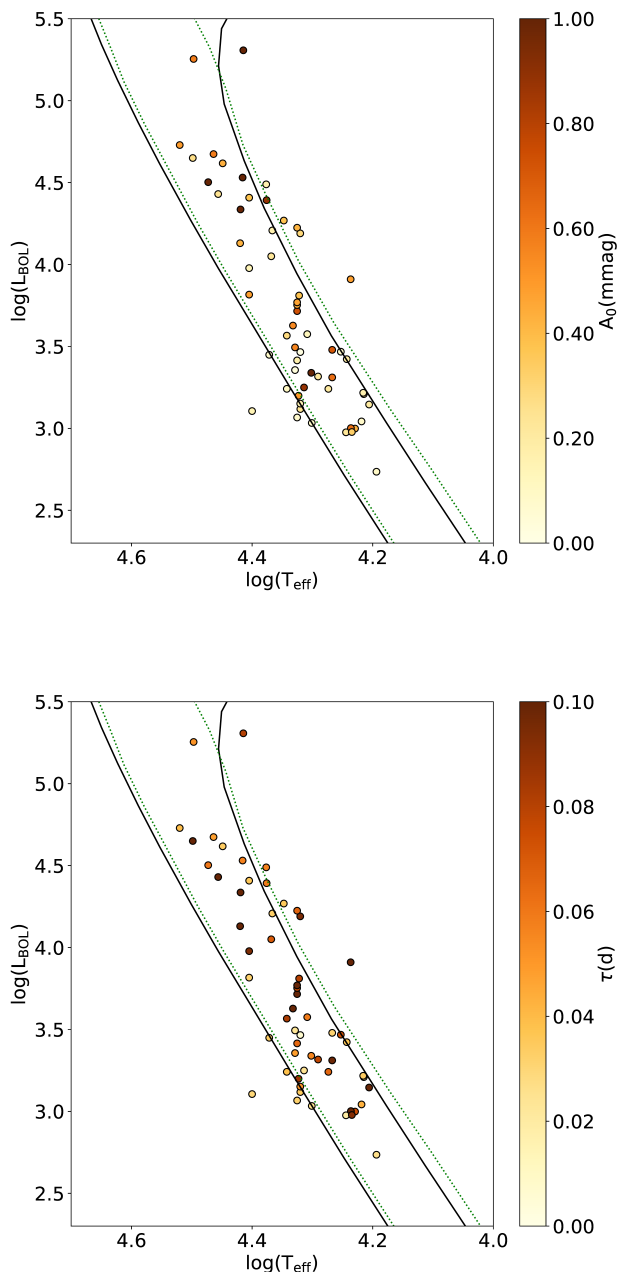


Fig. 4. Hertzsprung-Russell diagram. The symbol colours indicate the value of the red noise parameters A_0 and τ . The solid black and dotted green lines are the zero-age and terminal-age main sequences (ZAMS and TAMS) from Geneva stellar evolution models for solar abundance without and with rotation, respectively (Ekström et al. 2012).

4.2. Frequency groups with $f > 0.5 \text{ d}^{-1}$

As noted in previous section, typical FGs occur in the $0.5\text{--}6 \text{ d}^{-1}$ range. In previous observations of early-type stars, FGs were found with various amplitudes. This is also the case here. Indeed, several targets of our sample (e.g. HD5882, HD35532, HD252214, HD53755, HD68324, HD78548, HD87015, HD97499, HD97913, CPD-48 8710, HD180968, HD198781, and HD207308) display low-level FGs (i.e. FGs much fainter than other signals and often below significance). In contrast, 22 of our targets (i.e. about one-third of

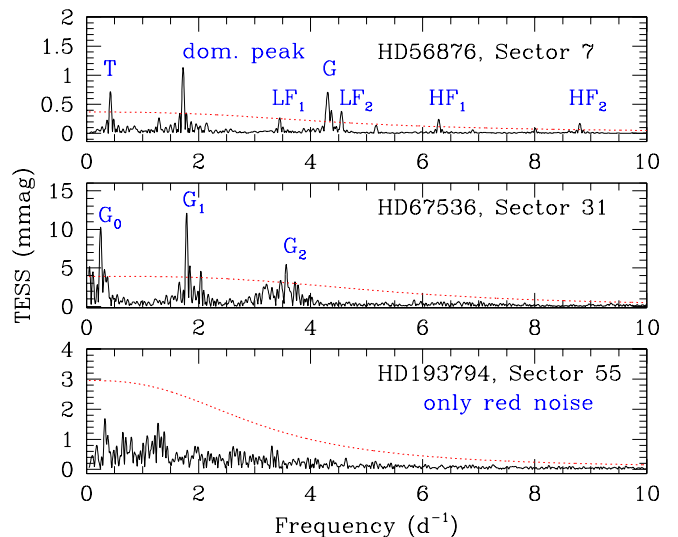


Fig. 5. Three examples of frequency spectra. HD 56876 displays red noise, long-term variations (peak labelled ‘T’ at $f < 0.5 \text{ d}^{-1}$), isolated signals at low and high frequencies (labelled ‘dom. peak’, LF_i , HF_i), and a small FG (labelled ‘G’). HD67536 displays FGs (labelled G_i) while HD193794 only displays red noise. The dashed curves correspond to the significance level, set to five times the noise level. Figures showing the full set of frequency spectra are available on Zenodo (see footnote 11).

the sample; see Table 1) display FGs that can be qualified as ‘strong’, that is, they dominate their frequency spectrum in the low-frequency range. This is in line with statistics from early Be stars (Balona & Ozuyar 2020; Nazé et al. 2020), although FGs in such stars are often even more impressive (e.g. broader, even more complex groups).

Of our 22 targets with FGs, only six (or 27% of the FG cases) show a single, strong group in the $0.5\text{--}6 \text{ d}^{-1}$ range. The majority of cases actually display at least two groups, usually noted G_1 and G_2 . Frequencies of G_1 groups range between 0.8 and 3.1 d^{-1} while those of G_2 groups are about twice larger (80% of cases have $f(G_2)/f(G_1)$ between 1.9 and 2.1). Again, this is fully in line with results obtained on Be stars (Labadie-Bartz et al. 2022). A difference with Be stars can be found when comparing amplitudes of the groups. In our sample, the G_1 groups display larger amplitudes than the G_2 groups in two-thirds of stars, while the remaining third mostly have a larger amplitude for G_2 groups (G_1 and G_2 groups with similar amplitudes are very rare). Be stars rather seem to split evenly between the three possibilities ($A(G_1) > A(G_2)$, $A(G_1) \sim A(G_2)$, $A(G_1) < A(G_2)$), with amplitude changes during flickers. It may also be interesting to note that additional groups are detected in 8 targets (33% of FG cases), with one case (HD68962) displaying groups up to extremely high frequencies. Finally, r-modes have been proposed to exist in fast-rotating stars (Saio et al. 2018). They can be found in a typical ‘hump and spike’ morphology in which a FG associated with the retrogrades r-modes (the ‘hump’) is complemented by a strong peak at its high-frequency limit (the ‘spike’, possibly corresponding to the rotational frequency). While a few cases are known in Be stars (Nazé et al. 2020; Labadie-Bartz et al. 2022), this morphology appear overall quite rare and this is also the case of our sample, for which none of the detected FGs display it.

In slowly pulsating B-type (SPB) stars (usually later than B3) and in γ Dor stars (mid-A to early F), FGs are commonly

interpreted as due to multi-mode pulsations (Van Reeth et al. 2015, 2016; Pápics et al. 2017; Pedersen et al. 2021). But in early B-stars, which are outside the standard SPB instability strip (as calculated for non-rotating stars), the origin of FGs is more debated. They may be considered as a consequence of fast rotation (Saio et al. 2018; Lee & Saio 2020), of changes in the circumstellar environment (i.e. decretion disks of Be stars, Baade et al. 2016), or of rotation of an inhomogeneous surface (Balona & Ozuyar 2020, 2021). Since our sample consists of stars that are fast-rotating but not known as Be stars (i.e. not known to have circumstellar disks), the second scenario appear less plausible. However, differences do exist with Be stars, notably regarding the amplitudes of the groups; hence, the circumstellar environment may possibly have a second-order impact, not on the presence of the groups themselves but on their morphologies.

4.3. Isolated signals with $f > 0.5 d^{-1}$

Isolated peaks are typical of stellar pulsations but they could also be related to rotation¹³ if the stellar surface is asymmetric (e.g. spots). Such peaks are also often detected in the frequency spectra of our targets (42 cases, or 72% of the sample; see the list in Table C.1). By ‘isolated’, we mean that these peaks clearly dominate their neighbourhood, that is to say, there are only much fainter peaks around, or no other peaks at all, beyond aliases of the main signal. It is usual to split such signals into low-frequencies ($0.5\text{--}6. d^{-1}$) and high frequencies ($6\text{--}15. d^{-1}$). This splitting is related to the nature of the pulsations, with low-frequencies most probably g-modes and high frequencies p-modes.

Nearly two-thirds of our sample (37 stars, or 64%) display isolated signals at low frequencies ($0.5\text{--}6. d^{-1}$). Such peaks may have low amplitudes but, in 24 cases (41% of the sample), the strongest signal recorded in the frequency spectrum is a peak, or a pair of peaks, in this range (hence our choice of a ‘dominant’ qualifier; see Col. 2 of Table C.1). Four additional stars (HD46883, HD87152, HD150745, and Cl* Berk. 86 HG 261) display a stronger signal at even lower frequencies (below $0.5 d^{-1}$) but isolated peaks in $0.5\text{--}6. d^{-1}$ dominate the spectra above $0.5 d^{-1}$, increasing the incidence of such dominant low-frequency signals to 48%. This is much larger than the fraction of 22.5% of early-type Be displaying isolated, low-frequency signals found by Labadie-Bartz et al. (2022) and is still above the larger, 20–40%, incidence found in Semaan et al. (2018), Balona & Ozuyar (2020), or Nazé et al. (2020).

Signals at higher frequencies ($6\text{--}15. d^{-1}$) are rarer: they are detected in 20 cases (34% of the sample). Such peaks are generally fainter than those at lower frequencies, with only 3 stars (HD68324, HD143118, and HD192968) having the largest-amplitude signals at high frequencies and 2 other targets (HD37303 and HD207308) displaying low and high-frequency peaks with similar amplitudes. This recalls the fraction of $\sim 10\%$ of early Be stars with strong high-frequency signals reported by Nazé et al. (2020) and Balona & Ozuyar (2020). Signals with even higher frequencies ($15\text{--}40. d^{-1}$) are found only in 11 cases (19% of the sample), again larger than the incidence of 2% found by Labadie-Bartz et al. (2022). Usually, such very high-frequency signals are quite faint: there is only one case (HD37303) with peaks of similar strengths at low, high, and very high frequencies.

¹³ The fundamental frequency is however limited by the critical rotation rate, about $3 d^{-1}$ for the targets.

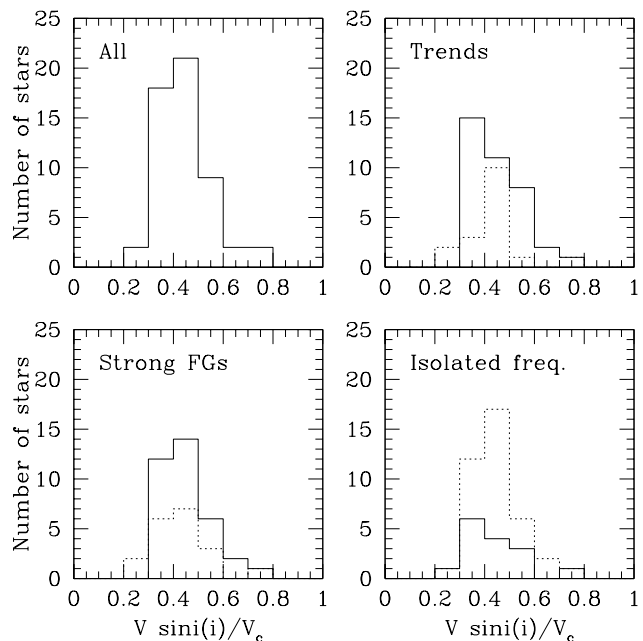


Fig. 6. Histograms of ratios $v \sin(i)/V_c$ for all targets (top-left panel) or targets separated by the type of signal recorded (trends on top right panel, strong FGs on bottom left panel, and isolated frequencies on bottom right panel). Cases with and without features are shown by dotted and solid lines, respectively.

The detected signals may not be independent. About 30% of the stars with isolated signals display harmonics (slightly fewer than one-half if taking close harmonics into account). For example, HD37397 displays several multiples ($2, 4, 6, 7,$ and $9 \times$) of the dominant signal at $1.744 d^{-1}$, as for HD35777 ($2, 4, 7, 9, 12,$ and $15 \times$ the dominant signal at $1.716 d^{-1}$), or HD37303 ($2, 7, 9,$ and $16 \times$ the dominant signal at $2.140 d^{-1}$). This is quite normal as, when using Fourier techniques, harmonics will naturally appear whenever the variability is not perfectly sinusoidal. It usually is more typical of rotational (e.g. David-Uraz et al. 2019) or binarity signals than of pulsations (Labadie-Bartz et al. 2020), though. Combination of frequencies can also be found in a few cases: in HD37674, the difference between 2.764 and $3.304 d^{-1}$ is similar to that between 6.076 and $6.612 d^{-1}$ or 12.144 and $12.664 d^{-1}$; in HD136298, the difference between 2.538 and $2.700 d^{-1}$ is also found between 4.710 and $4.870 d^{-1}$ while that between 8.580 and $9.770 d^{-1}$ resembles that between 10.576 and $11.746 d^{-1}$.

Figure 6 shows histograms of observed criticality ratios $v \sin(i)/V_c$ for all targets as well as targets displaying (or not) some feature. As can be seen, there is no significant difference between the samples with or without the chosen features (trends, strong FGs, isolated signals). No physical correlation between one feature and rotation can thus be derived. Figure 7 shows the targets, with symbols coding their variability type, in a Hertzsprung-Russell diagram with instability zones indicated. Targets appear between the ZAMS and the TAMS, as could be expected. Targets with high-frequency signals (asterisk or filled symbols) do not appear clearly separated from targets with only low-frequency signals (open symbols). High-frequency pulsators are even found far out of the β Cep area. Of course, uncertainties on temperatures and bolometric luminosities can be expected as fast rotation and unknown viewing angle could bias the estimates of these quantities (see also Section 2).

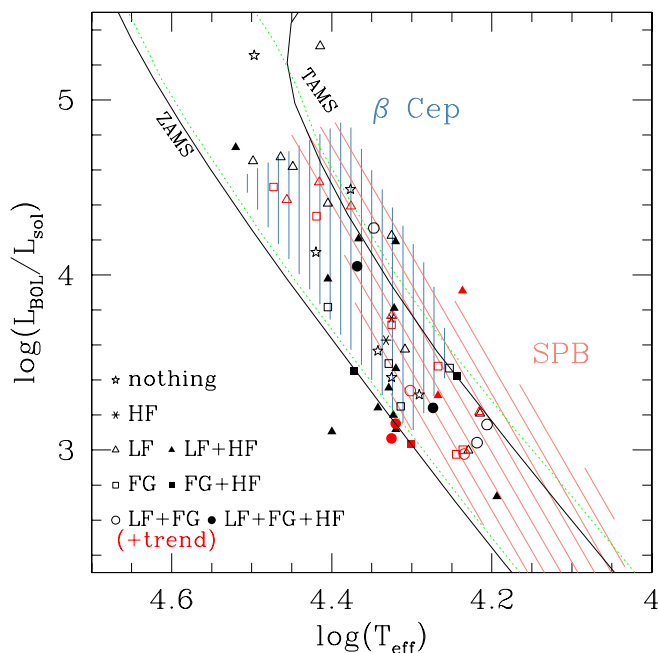


Fig. 7. Hertzsprung-Russell diagram. The symbols depict the type of variability and have the same meanings as in Fig. 3. The solid black and dotted green lines are the ZAMS and TAMS from Geneva stellar evolution models for solar abundance without and with rotation, respectively (Ekström et al. 2012; see our Fig. 4). The hatched areas mark the instability zones of β Cep and SPB stars from Miglio et al. (2007).

In addition, detailed asteroseismic modelling would be required to better understand the behaviour of these objects.

5. Conclusions

Fast-rotating OB stars come in two flavours, those with disks (also known as Oe/Be stars) and those without disks. The variability of the former group has been repeatedly examined over the years, while the latter group benefited from less attention. Using data from TESS and *Kepler*, we report here a detailed photometric study of 58 isolated, early-type ($>B3$), fast-rotating ($v \sin(i) > 200 \text{ km s}^{-1}$) massive stars not known to display disks. This work aims at identifying the similarities and differences in the variability patterns of rapidly rotating early B-type stars with and without the Be phenomenon. The difference in behaviour may provide clues as to which variability is typical of circumstellar matter and which is not, providing guidance for future modelling.

The presence of white+red noise is ubiquitous in our sample, as in OB stars in general. Telescope sensitivity limits the detection of faint white noise, and red noise always appear stronger than white noise in our targets. Correlations between different red noise parameters and between these parameters and stellar properties were searched for, but none could be found.

Signals significantly above the noise level are detected in 90% of the sample but such variability occurs on very different timescales. First, 20–30% of stars in our sample are affected by long-term changes, which even dominate the frequency spectra for 12% of the total sample. There is clearly a lower incidence of long-term variability, caused by isolated peaks or very low-frequency frequency groups (G_0), in our sample than in Be stars, underlining the role of circumstellar changes on long-term variability.

Strong FGs are detected in 38% of our sample, often with two or more groups forming a near-harmonic series (e.g. $f(G_2) \sim 2f(G_1)$), as in Be stars. In other words, the occurrence of FGs may somehow be linked to fast rotation but it is clearly not sufficient to classify a star as a Be type since FGs can also be found in fast-rotating non-Be stars. Moreover, this also implies that FGs do not appear to be a crucial factor for the Be phenomenon (i.e. for the creation of a disk). However, in our sample, the first FG most often displays the largest amplitude, unlike in Be stars. This difference in the relative strengths of FGs in the Be versus non-Be stars suggests that, while not being fully dependent on each other, some interplay exists between the circumstellar environment and these groups.

Isolated signals are frequent in our sample, especially in the $0.5\text{--}6 \text{ d}^{-1}$ range: two-thirds of our stars display such low-frequency signals and these signals even dominate the frequency spectrum for 41% of our sample. Both of these rates are higher than what is found for Be stars. Higher-frequency signals also are more frequent in our sample than in Be stars, although they are rarely dominating (this concerns only 9% of our cases). It should be noted that the presence of high-frequency signals is not limited to stars in the β Cep locus.

While variability patterns are now identified, much remains to be done. First, our conclusions would be strengthened by an in-depth spectroscopic analysis of our sample stars. High-quality spectra, coupled with atmosphere modelling of distorted stars, would allow us to determine the stellar properties more precisely. A sparse monitoring of our targets could also be useful, to assess whether some of them display emission lines at some point (the Be phenomenon may be intermittent). Finally, high-cadence spectroscopic monitoring would further allow us to identify the spectroscopic variability features associated to the photometric changes. The next step would then be to perform a detailed asteroseismic modelling of stars with and without disks using the derived constraints.

Overall, one still needs to identify what makes a Be star so special. While one could expect a strong impact on its behaviour due to the presence of circumstellar material, this work demonstrates that Be and non-Be stars actually share many similarities in their photometric properties. This may not be entirely surprising as, for some Be stars, the overall properties of the frequency spectra do not seem to depend on the disk size (see Appendix D). Photometric data thus seem more sensitive to the occurrence of ejection events than the simple presence or absence of a circumstellar disk. This is particularly intriguing as the presence of Be disks has been proposed to be linked to specific pulsational behaviour (e.g. Huat et al. 2009). One additional ingredient should probably be considered, such as how strong or common mode coupling is. Fast rotation is definitely not sufficient to explain the occurrence of the Be phenomenon, and neither is the presence of photometric FGs.

Acknowledgements. The authors acknowledge the referee, J. Zorec, for his interesting comments and S; Ekström for help with her evolutionary models. Y.N. acknowledges support from the Fonds National de la Recherche Scientifique (Belgium), the European Space Agency (ESA) and the Belgian Federal Science Policy Office (BELSPO) in the framework of the PRODEX Programme (contracts linked to XMM-Newton and Gaia). N.B. acknowledges support from the Belgian federal government grant for Ukrainian postdoctoral researchers (contract UF/2022/10). This paper includes data collected by the TESS mission, which are publicly available from the Mikulski Archive for Space Telescopes (MAST). Funding for the TESS mission is provided by NASA’s Science Mission Directorate. This paper includes data collected by the Kepler mission and obtained from the MAST data archive at the Space Telescope Science Institute (STScI). This work makes use of observations from the Las Cumbres Observatory global telescope network. This work uses observations obtained at the Dominion Astrophysical Observatory, NRC Herzberg, Programs in Astronomy and Astrophysics,

National Research Council of Canada. ADS and CDS were used for preparing this document.

References

- Abt, H. A., Levato, H., & Grosso, M. 2002, *ApJ*, 573, 359.
- Alexander, M. J., Hanes, R. J., Povich, M. S., et al. 2016, *AJ*, 152, 190.
- Anderson, E. & Francis, C. 2012, *Astronomy Letters*, 38, 331.
- Baade, D., Rivinius, T., Pigulski, A., et al. 2016, *A&A*, 588, A56.
- Bailer-Jones, C. A. L., Rybizki, J., Foesneau, M., et al. 2021, *AJ*, 161, 147.
- Balona, L. A. 1975, *MmRAS*, 78, 51
- Balona, L. A., Handler, G., Chowdhury, S., et al. 2019, *MNRAS*, 485, 3457.
- Balona, L. A. & Ozuyar, D. 2020, *MNRAS*, 493, 2528.
- Balona, L. A. & Ozuyar, D. 2021, *ApJ*, 921, 5.
- Baran, A. S., Koen, C., & Pokrzywka, B. 2015, *MNRAS*, 448, L16
- Berghoefter, T. W., Schmitt, J. H. M. M., & Cassinelli, J. P. 1996, *A&AS*, 118, 481
- Blomme, R., Mahy, L., Catala, C., et al. 2011, *A&A*, 533, A4
- Bourgés, L., Lafrasse, S., Mella, G., et al. 2014, *Astronomical Data Analysis Software and Systems XXIII*, 485, 223
- Bowman, D. M., Burssens, S., Pedersen, M. G., et al. 2019, *Nature Astronomy*, 3, 760
- Bowman, D.M., Burssens, S., Simón-Díaz, S., et al. 2020, *A&A*, 640, A36
- Bragança, G. A., Daffon, S., Cunha, K., et al. 2012, *AJ*, 144, 130.
- Briquet, M., Hubrig, S., De Cat, P., et al. 2007, *A&A*, 466, 269.
- Britavskiy, N., Simón-Díaz, S., Holgado, G., et al. 2023, *A&A*, 672, A22.
- Brown, A. G. A. & Verschueren, W. 1997, *A&A*, 319, 811.
- Brown, T. M., Baliber, N., Bianco, F. B., et al. 2013, *PASP*, 125, 1031.
- Burssens, S., Simón-Díaz, S., Bowman, D. M., et al. 2020, *A&A*, 639, A81.
- Cazorla, C., Morel, T., Nazé, Y., et al. 2017, *A&A*, 603, A56.
- Cochetti, Y. R., Zorec, J., Cidale, L. S., et al. 2020, *A&A*, 634, A18.
- Currie, T., Hernandez, J., Irwin, J., et al. 2010, *ApJS*, 186, 191.
- Cuyper, J., Balona, L. A., & Marang, F. 1989, *A&AS*, 81, 151
- Daffon, S., Cunha, K., de Araújo, F. X., et al. 2007, *AJ*, 134, 1570.
- David, T. J. & Hillenbrand, L. A. 2015, *ApJ*, 804, 146.
- David-Uraz, A., Neiner, C., Sikora, J., et al. 2019, *MNRAS*, 487, 304.
- de Mink, S. E., Langer, N., Izzard, R. G., et al. 2013, *ApJ*, 764, 166.
- Ekström, S., Georgy, C., Eggenberger, P., et al. 2012, *A&A*, 537, A146.
- Fitzpatrick, E. L. & Massa, D. 2007, *ApJ*, 663, 320.
- Frémat, Y., Zorec, J., Hubert, A.-M., et al. 2005, *A&A*, 440, 305.
- Garmany, C. D., Glaspey, J. W., Bragança, G. A., et al. 2015, *AJ*, 150, 41.
- Ghoreyshi, M. R., Carciofi, A. C., Jones, C. E., et al. 2021, *ApJ*, 909, 149.
- Głęboccki, R. & Gnaniński, P. 2005, 13th Cambridge Workshop on Cool Stars, Stellar Systems and the Sun, 560, 571
- Gosset, E., Royer, P., Rauw, G., et al. 2001, *MNRAS*, 327, 435.
- Guetter, H. H. 1976, *AJ*, 81, 537.
- Gullikson, K., Kraus, A., & Dodson-Robinson, S. 2016, *AJ*, 152, 40.
- Gutiérrez-Soto, J., Fabregat, J., Suso, J., et al. 2007, *A&A*, 476, 927.
- Hanes, R. J., McSwain, M. V., & Povich, M. S. 2018, *AJ*, 155, 190.
- Harvey, J. 1985, *Future Missions in Solar, Heliospheric & Space Plasma Physics*, 235, 199
- Heck, A., Manfroid, J., & Mersch, G. 1985, *A&AS*, 59, 63
- Hernández, J., Calvet, N., Hartmann, L., et al. 2005, *AJ*, 129, 856.
- Hohle, M. M., Neuhäuser, R., & Schutz, B. F. 2010, *Astronomische Nachrichten*, 331, 349.
- Howarth, I. D., Siebert, K. W., Hussain, G. A. J., et al. 1997, *MNRAS*, 284, 265.
- Huang, W. & Gies, D. R. 2006a, *ApJ*, 648, 580.
- Huang, W. & Gies, D. R. 2006b, *ApJ*, 648, 591.
- Huang, W., Gies, D. R., & McSwain, M. V. 2010, *ApJ*, 722, 605.
- Huat, A.-L., Hubert, A.-M., Baudin, F., et al. 2009, *A&A*, 506, 95.
- Hubert, A. M. & Floquet, M. 1998, *A&A*, 335, 565
- Hubrig, S., Briquet, M., De Cat, P., et al. 2009, *Astronomische Nachrichten*, 330, 317.
- Kallinger, T., Reegen, P., & Weiss, W. W. 2008, *A&A*, 481, 571.
- Keller, S. C., Bessell, M. S., Cook, K. H., et al. 2002, *AJ*, 124, 2039.
- Kervella, P., Arenou, F., & Thévenin, F. 2022, *A&A*, 657, A7.
- Kharchenko, N. V. 2001, *Kinematika i Fizika Nebesnykh Tel.* 17, 409
- Klement, R., Carciofi, A. C., Rivinius, T., et al. 2019, *ApJ*, 885, 147.
- Labadie-Bartz, J., Pepper, J., McSwain, M. V., et al. 2017, *AJ*, 153, 252.
- Labadie-Bartz, J., Handler, G., Pepper, J., et al. 2020, *AJ*, 160, 32.
- Labadie-Bartz, J., Carciofi, A. C., Henrique de Amorim, T., et al. 2022, *AJ*, 163, 226.
- Lallement, R., Vergely, J.-L., Valette, B., et al. 2014, *A&A*, 561, A91.
- Lee, U. & Saio, H. 2020, *MNRAS*, 497, 4117.
- Levenhagen, R. S. & Leister, N. V. 2006, *MNRAS*, 371, 252.
- Marsh Boyer, A. N., McSwain, M. V., Aragona, C., et al. 2012, *AJ*, 144, 158.
- Melnik, A. M. & Dambis, A. K. 2020, *MNRAS*, 493, 2339.
- Mennickent, R. E., Pietrzyński, G., Gieren, W., et al. 2002, *A&A*, 393, 887.
- Miglio, A., Montalbán, J., & Dupret, M.-A. 2007, *Communications in Asteroseismology*, 151, 48.
- Monin, D., Saddlemyer, L., & Bohlender, D. 2014, *Revista Mexicana de Astronomia y Astrofisica Conference Series*, 45, 69
- Nazé, Y., Rauw, G., & Pigulski, A. 2020, *MNRAS*, 498, 3171.
- Nazé, Y., Rauw, G., & Gosset, E. 2021, *MNRAS*, 502, 5038.
- Neiner, C., de Batz, B., Cochard, F., et al. 2011, *AJ*, 142, 149.
- Pápics, P. I., Tkachenko, A., Van Reeth, T., et al. 2017, *A&A*, 598, A74.
- Paunzen, E., Schnell, A., & Maitzen, H. M. 2005, *A&A*, 444, 941.
- Pecaut, M. J. & Mamajek, E. E. 2013, *ApJS*, 208, 9.
- Pedersen, M. G., Escorza, A., Pápics, P. I., et al. 2020, *MNRAS*, 495, 2738.
- Pedersen, M. G., Aerts, C., Pápics, P. I., et al. 2021, *Nature Astronomy*, 5, 715.
- Penny, L. R. & Gies, D. R. 2009, *ApJ*, 700, 844.
- Peton-Jonas, D. 1981, *A&AS*, 45, 193
- Pope, B. J. S., White, T. R., Farr, W. M., et al. 2019, *ApJS*, 245, 8.
- Rauw, G., Pigulski, A., Nazé, Y., et al. 2019, *A&A*, 621, A15
- Ricker, G. R., Winn, J. N., Vanderspek, R., et al. 2015, *Journal of Astronomical Telescopes, Instruments, and Systems*, 1, 014003
- Rivinius, T., Carciofi, A. C., & Martayan, C. 2013, *A&A Rev.*, 21, 69.
- Rogers, T.M., Lin, D.N.C., McElwaine, J.N., & Lau, H.B.B. 2013, *ApJ*, 772, 21
- Saio, H., Bedding, T. R., Kurtz, D. W., et al. 2018, *MNRAS*, 477, 2183.
- Saio, H., Kurtz, D. W., Murphy, S. J., et al. 2018, *MNRAS*, 474, 2774.
- Semaan, T., Hubert, A. M., Zorec, J., et al. 2018, *A&A*, 613, A70.
- Sigut, T. A. A. & Patel, P. 2013, *ApJ*, 765, 41.
- Simón-Díaz, S. & Herrero, A. 2014, *A&A*, 562, A135.
- Shao, Y. & Li, X.-D. 2014, *ApJ*, 796, 37.
- Soubiran, C., Le Campion, J.-F., Broillet, N., et al. 2016, *A&A*, 591, A118.
- Stankov, A. & Handler, G. 2005, *ApJS*, 158, 193.
- Strom, S. E., Wolff, S. C., & Dror, D. H. A. 2005, *AJ*, 129, 809.
- Teltng, J. H., Schrijvers, C., Ilyin, I. V., et al. 2006, *A&A*, 452, 945.
- Tetzlaff, N., Neuhäuser, R., & Hohle, M. M. 2011, *MNRAS*, 410, 190.
- van Belle, G. T. 2012, *A&A Rev.*, 20, 51.
- van Bever, J. & Vanbeveren, D. 1997, *A&A*, 322, 116
- Van Reeth, T., Tkachenko, A., Aerts, C., et al. 2015, *ApJS*, 218, 27.
- Van Reeth, T., Tkachenko, A., & Aerts, C. 2016, *A&A*, 593, A120.
- Wang, L., Gies, D. R., Peters, G. J., et al. 2021, *AJ*, 161, 248.
- Wegner, W. 2003, *Astronomische Nachrichten*, 324, 219.
- Wolff, S. C., Strom, S. E., Dror, D., et al. 2007, *AJ*, 133, 1092.
- Wu, Y., Singh, H. P., Prugniel, P., et al. 2011, *A&A*, 525, A71.
- Xiang, M., Rix, H.-W., Ting, Y.-S., et al. 2022, *A&A*, 662, A66.
- Xu, Y., Bian, S. B., Reid, M. J., et al. 2018, *A&A*, 616, L15.
- Xu, Y., Hou, L. G., Bian, S. B., et al. 2021, *A&A*, 645, L8.
- Yudin, R. V. 2001, *A&A*, 368, 912.
- Zechmeister, M. & Kürster, M. 2009, *A&A*, 496, 577.
- Zhang, P., Chen, P. S., & Yang, H. T. 2005, *New A*, 10, 325.
- Zorec, J. 2023, *Galaxies*, 11, 54.

Appendix A: Target list**Appendix B: Red noise parameters****Appendix C: Properties of isolated signals****Appendix D: A note on the Be stars 25 Ori, 25 Cyg and V434 Aur**

In order to assess potential contributions to photometric signals from circumstellar material, spectroscopic observations were taken of select Be stars during their TESS observing windows. The spectroscopy can then be used to infer whether or not any disk was present during the TESS observations (see Labadie-Bartz et al., in preparation). Two example Be stars observed in this fashion, 25 Ori and V434 Aur, are shown in Fig. D.1. For 25 Ori, the spectra show strong $H\alpha$ emission, indicating the presence of a dense disk, while for V434 Aur there is no emission in $H\alpha$ (nor in any other lines) indicating that no disk was present at the time of TESS observations. However, the light curves and frequency spectra of these two stars are qualitatively the same, despite 25 Ori having a strong disk, and V434 Aur having no disk.

A similar comparison can be made for observations of the same star, 25 Cyg, in two different TESS sectors (Fig. D.2). During Sector 41, the system had no emission (and is thus without any disk material). In Sectors 54 and 55, $H\alpha$ displayed weak emission, indicating a low density (dissipating) disk. The photometric variability at these two epochs is essentially the same, with only mild variations in the strength of certain frequencies, but the overall structure of the FGs remains the same. This suggests that for this star, the presence of a (weak) disk has no major impact on the signals encoded in TESS.

The spectroscopic data used in the above examples were taken with two different instruments. Echelle spectra were obtained with the Network of Robotic Echelle Spectrographs (NRES, $R \sim 53000$) attached to the 1 m telescopes of the Las Cumbres Observatory Global Telescope network (Brown et al. 2013), including at the Wise observatory, the South African Astronomical Observatory, and McDonald Observatory. Observations were also obtained from the Dominion Astrophysical Observatory (DAO) 1.2m telescope equipped with the McKeller spectrograph (with resolving power $R \sim 17600$), which covers $H\alpha$ and $He\text{I } \lambda 6678$ in the chosen observing mode (Monin et al. 2014).

Table A.1. Target list, ordered by increasing RA.

Name	Sectors	TIC	$d(\text{pc})$	SpT	Ref.	$v \sin(i)$ (km s^{-1})	Ref.	$T_{\text{eff}}(\text{K})$	Ref.	$\log(L_{\text{BOL}}/L_{\odot})$	$v \sin(i)/V_c$
HD5882	17,18,58	299328900	423.7±7.7	B2.5Vn	Xu et al. (2021)	358	Huang et al. (2010)	15624	Huang et al. (2010)	2.74	0.60
NGC 869 133	18,58	348137277	2555.6±279.3			341	Marsh Boyer et al. (2012)	17500	Marsh Boyer et al. (2012)	3.42	
BD+56 538	18,58*	348231861	2221.3±70.0	B2	Xu et al. (2021)	235	Marsh Boyer et al. (2012)	20900	Marsh Boyer et al. (2012)	4.19	0.61
HD14250	18*,58	348314700	2485.1±585.9	B1V	Currie et al. (2010)	236	Huang & Gies (2006b)	25972	Huang & Gies (2006b)	5.31	0.77
BD+62 657	19,59*,73*	84429626	1015.0±18.2	B2V	Xu et al. (2021)	212	Huang & Gies (2006b)	23347	Huang & Gies (2006b)	4.05	0.46
HD34748	5,32*	4011607	358.8±11.2	B1.5V	Paunzen et al. (2005)	295	Cochetti et al. (2020)	23529	Cochetti et al. (2020)	3.45	0.38
HD35532	6*,32*,43*,44*,45*,71*	302267223	333.6±7.9	B2Vn	Abt et al. (2002)	281	Huang et al. (2010)	16397	Huang et al. (2010)	3.21	0.53
HD35777	6,32*	50524860	344.3±5.9	B2V	Hohle et al. (2010)	230	Bragança et al. (2012)	22000	Hohle et al. (2010)	3.24	0.33
HD37303	6*,32*	332856560	362.9±9.8	B1.5V	Burssens et al. (2020)	280	Burssens et al. (2020)	20893	Burssens et al. (2020)	3.47	0.41
HD37397	6,32	11199427	345.8±6.6	B2V	Bragança et al. (2012)	236	Bragança et al. (2012)	20893	Hernández et al. (2005)	3.12	0.33
HD37674	6	11299576	404.5±6.5	B5Vn	Guetter (1976)	385	Głębocki & Gnaciński (2005)	25119	Hernández et al. (2005)	3.10	
HD249845	19,43*,44*,45*,71*,72*,73*	353298304	796.5±23.6	B2:V:nn	Anderson & Francis (2012)	218	Głębocki & Gnaciński (2005)	20600 ^m		3.25	0.34
HD252214	6,33,43*,44*,71*,72*	59468295	920.7±29.3	B2.5V	Anderson & Francis (2012)	280	Głębocki & Gnaciński (2005)	20350	Hohle et al. (2010)	3.57	0.58
HD254042	71,72	83017766	1629.9±54.7	B0.5:IV:nn	Xiang et al. (2022)	226	Xiang et al. (2022)	22253	Xiang et al. (2022)	4.27	0.40
HD259865	6,33	234951915	1311.8±31.7	B5V	Bourgés et al. (2014)	256	Huang & Gies (2006b)	18773	Huang & Gies (2006b)	3.24	
HD46994	6*,7*,33*	172233421	860.7±30.0	B2/3V	Bragança et al. (2012)	271	Bragança et al. (2012)	21320	Bragança et al. (2012)	3.49	0.51
HD46883	6,33	220134169	1123.3±34.4	B0.5:V	Xu et al. (2018)	227	Głębocki & Gnaciński (2005)	23764	Fitzpatrick & Massa (2007)	4.39	0.41
HD47360	6,33	319854134	1319.9±57.4	B0.5V	Melnik & Dambis (2020)	237	Daflon et al. (2007)	26250	Daflon et al. (2007)	4.34	0.37
HD52463	6,7,33,34	63359889	831.1±22.3	B3V	Bragança et al. (2012)	262	Bragança et al. (2012)	16540	Bragança et al. (2012)	3.04	0.52
HD53755	7,33*	177129056	1050.4±43.3	B0.5V	Wegner (2003)	285	Cazorla et al. (2017)	28100	Cazorla et al. (2017)	4.62	0.49
HD56876	7*,33*,34*,61*	66594335	279.7±3.0	B2IV	Hohle et al. (2010)	310	Abt et al. (2002)	21150	Hohle et al. (2010)	3.07	0.42
ALS 864	7,8,34,61	129364127	4054.6±399.1	B0V	Peton-Jonas (1981)	249	Cazorla et al. (2017)	31500	Cazorla et al. (2017)	4.65 ^m	0.36
HD67536	1,4*,7*,8*,9*,10*,11,28*,31*,34*,35*,37*,38*,61*,62*,63*,64*,68*,69*	308542383	419.9±7.3	B2.5Vn	Stankov & Handler (2005)	325	Głębocki & Gnaciński (2005)	18500 ^m		3.48	0.70
HD68217	7*,8*,34*,35*,61*,62*	354931043	329.6±15.9	B2IV	Hohle et al. (2010)	214	Głębocki & Gnaciński (2005)	21150	Hohle et al. (2010)	3.72	0.42
HD68324	7*,8*,9*,34*,35*,61*,62*	238612881	342.5±8.9	B2IV	Stankov & Handler (2005)	210	Głębocki & Gnaciński (2005)	21150	Hohle et al. (2010)	3.75	0.42
HD68962	7*,8*,34*,35*,61*	182315791	460.9±7.6	B2/3V	Bragança et al. (2012)	293	Bragança et al. (2012)	17550	Bragança et al. (2012)	2.98	0.50
HD75869	8,35,62	190264184	589.5±12.4	B2V	Hohle et al. (2010)	208	Balona (1975)	22000	Hohle et al. (2010)	3.57	0.36
HD78548	8,10,35*,37*,62*,63*	384642833	342.1±8.8	B2IV	Hohle et al. (2010)	215	Balona (1975)	21150	Hohle et al. (2010)	3.41	0.36
HD81347	9,35,36,62,63	295691515	479.1±9.8	B3IV	Hohle et al. (2010)	250	Balona (1975)	17900	Hohle et al. (2010)	3.47	0.58
HD87015	21*,45*,46*,48*,72*	26987416	308.3±7.9	B2.5IV	Teltung et al. (2006)	215	Teltung et al. (2006)	16435	Huang et al. (2010)	3.22	0.43
HD87152	9,10,36*,37*,63*	134730105	361.0±8.1	B2.5V	Berghoefer et al. (1996)	236	Balona (1975)	18500 ^m		3.31	0.46
HD93501	10,11,36,37,63,64	391527871	1880.1±73.6	B0V	Alexander et al. (2016)	210	Hanes et al. (2018)	29700	Alexander et al. (2016)	4.50	0.30
HD97499	10,11,37,64	467235690		B0.5	Melnik & Dambis (2020)	201	Daflon et al. (2007)	28590	Daflon et al. (2007)	4.43 ^m	0.33
HD97913	10,11,37,64*	450359616	2612.5±148.7	B0.5IVn	Bragança et al. (2012)	326	Bragança et al. (2012)	33110	Bragança et al. (2012)	4.73	0.51
HD108257	10*,11*,37*	260646994	135.6±2.7	B3Vn	Gullikson et al. (2016)	298	Wolff et al. (2007)	20000	Gullikson et al. (2016)	3.03	0.48
HD125238	11*,38*,65*	242497929	107.9±5.2	B2.5IV	Brown & Verschueren (1997)	222	van Belle (2012)	19525	Hohle et al. (2010)	3.32	0.40
HD133385	12,38,39,65,66	403073918	1049.1±36.4	B2Vn	Tetzlaff et al. (2011)	257	Balona (1975)	21150	Hohle et al. (2010)	4.22	0.68
HD136298	11*,38*,65*	148415949	149.8±13.6	B1.5IV	van Belle (2012)	225	van Belle (2012)	20990	Soubiran et al. (2016)	3.81	0.40
HD138485	KEPLER	ktwo200194914	229.4±6.6	B2Vn	Strom et al. (2005)	203	Bragança et al. (2012)	21320	Bragança et al. (2012)	3.36	0.32
HD142378	KEPLER	ktwo205104403	264.6±27.7	B1.5Vn	Gullikson et al. (2016)	225	Strom et al. (2005)	16069	Briquet et al. (2007)	3.15	0.36
HD143118	12*,65*	59095516	131.6±7.2	B2.5V	van Belle (2012)	240	van Belle (2012)	21490	Soubiran et al. (2016)	3.63	0.49
CPD-50 9216	12,39,66	315368472	1849.3±54.5	B0.5IV	Kharchenko (2001)	230	Daflon et al. (2007)	20040	Daflon et al. (2007)	3.34	0.27
CPD-48 8710	12,39,66	39645989	1135.0±28.2	B0.5V	Kharchenko (2001)	296	Huang & Gies (2006b)	21036	Huang & Gies (2006b)	3.20	0.30
HD150745	12*,39*,66*	420629395	403.5±11.8	B2IV	Hohle et al. (2010)	244	Głębocki & Gnaciński (2005)	21150	Hohle et al. (2010)	3.77	0.49
HD164900	40*,53*	462709664	281.8±4.1	B3Vn	Paunzen et al. (2005)	260	Cochetti et al. (2020)	16954	Cochetti et al. (2020)	3.00	0.49
HD166197	13,66*	57997895	982.3±72.2	B1V	Berghoefer et al. (1996)	229	Hubrig et al. (2009)	23800	Hubrig et al. (2009)	4.49	0.51
HD168905	13*,66*	89975465	178.0±4.1	B2.5V	Hohle et al. (2010)	248	Cochetti et al. (2020)	20901	Cochetti et al. (2020)	3.15	0.39
HD180968	14*,40*,54*	354462452	544.9±23.6	B0.5IV	Abt et al. (2002)	270	Abt et al. (2002)	26043	Wu et al. (2011)	4.53	0.48
HD192968	14,15,41*,55*	11345334	982.6±32.4	B1Vne	Hohle et al. (2010)	287	Głębocki & Gnaciński (2005)	25400	Hohle et al. (2010)	3.98	0.44
CI* Berkeley											
86 HG 261	14,15,41,55	274068655	1695.6±29.8	B1.5V	Huang & Gies (2006a)	251	Huang & Gies (2006b)	17241	Huang & Gies (2006b)	3.91 ^m	0.58
HD193794	14,15,41*,55*	13116289	2086.0±226.3	B0V	Zhang et al. (2005)	231	Głębocki & Gnaciński (2005)	31400 ^m		5.25	0.48
HD198781	15*,17*,18*,24*,56*,57*,58*	305255878	922.7±20.3	B0.5V	Berghoefer et al. (1996)	222	Cazorla et al. (2017)	29100	Cazorla et al. (2017)	4.67	0.38
HD201819	15*,55*,56*	166354242	978.2±44.7	B0.5IVn	Xu et al. (2021)	215	Abt et al. (2002)	25400	Hohle et al. (2010)	4.41	0.37
HD207308	16,17,24,56,57,58	408100370	907.7±14.3	B0.7III-IV(n)	Anderson & Francis (2012)	207	Daflon et al. (2007)	23250	Daflon et al. (2007)	4.21	0.37
LS III +57 89	16,17	343878178	2854.2±188.7	B1V	Wolff et al. (2007)	204	Huang et al. (2010)	26291	Huang et al. (2010)	4.13 ^m	0.33
HD216092	16,17,56,57	66964209	874.6±78.4	B1.5Vn	Anderson & Francis (2012)	261	Głębocki & Gnaciński (2005)	25400	Hohle et al. (2010)	3.82	0.39
NGC 7654 485	17,18,24,57,58	269518687	1743.5±27.2			232	Huang et al. (2010)	17225	Huang et al. (2010)	3.00	
HD223145	1*,2*,28*,29*,68*,69*	206362352	180.9±2.7	B2.5V	Balona et al. (2019)	240	Balona et al. (2019)	17163	Balona et al. (2019)	2.98	0.42

Notes. A star after the sector's number indicates a high-cadence TESS observation, ^m indicates a value from Mamajek's stellar calibration.

Table B.1. Red noise parameters for all light curves.

Name	Sector	$C(\text{mmag})$	$A_0(\text{mmag})$	$\tau(\text{d})$	γ
HD5882	17	0.0172±0.0022	0.087±0.006	0.0369±0.0025	4.11±0.95
HD5882	18	0.0143±0.0024	0.087±0.007	0.0343±0.0024	4.37±1.07
HD5882	58	0.0055±0.0002	0.091±0.002	0.0262±0.0007	2.64±0.11
NGC 869 133	18	0.0302±0.0312	0.827±0.328	0.4285±0.4350	0.69±0.21
NGC 869 133	58	0.0360±0.0005	0.199±0.006	0.0366±0.0014	2.71±0.17
BD+56 538	18	0.0405±0.0032	0.384±0.026	0.1567±0.0157	1.94±0.23
BD+56 538	58*	0.0133±0.0001	0.296±0.004	0.0949±0.0017	2.53±0.07
HD14250	18*	0.0289±0.0005	1.142±0.015	0.0809±0.0017	1.76±0.03
HD14250	58	0.0223±0.0007	0.904±0.015	0.0776±0.0020	1.83±0.04
BD+62 657	19	0.0273±0.0018	0.198±0.009	0.0799±0.0039	3.95±0.57
BD+62 657	59*	0.0092±0.0002	0.158±0.004	0.0663±0.0030	1.42±0.04
BD+62 657	73*	0.0095±0.0002	0.226±0.006	0.0703±0.0037	1.28±0.04
HD34748	5	-0.0078±0.0108	0.109±0.020	0.0315±0.0052	1.26±0.35
HD34748	32*	0.0028±0.0001	0.083±0.001	0.0337±0.0010	1.70±0.04
HD35532	6*	0.0102±0.0003	0.419±0.005	0.0302±0.0005	2.65±0.07
HD35532	32*	0.0038±0.0002	0.160±0.002	0.0324±0.0005	3.95±0.17
HD35532	43*	0.0034±0.0002	0.162±0.002	0.0281±0.0005	3.08±0.12
HD35532	44*	0.0036±0.0002	0.175±0.002	0.0284±0.0005	3.07±0.11
HD35532	45*	0.0037±0.0002	0.198±0.003	0.0304±0.0006	2.71±0.10
HD35532	71*	0.0042±0.0003	0.280±0.004	0.0292±0.0005	2.62±0.08
HD35777	6	0.0259±0.0019	0.087±0.005	0.0366±0.0010	18.5±8.14
HD35777	32*	0.0040±0.0001	0.102±0.001	0.0384±0.0002	23.9±2.46
HD37303	6*	0.0025±0.0001	0.022±0.001	0.0148±0.0009	1.40±0.07
HD37303	32*	0.0028±0.0001	0.012±0.001	0.0067±0.0001	4.32±0.27
HD37397	6	0.0554±0.0041	0.244±0.011	0.0391±0.0006	41.3±22.0
HD37397	32	0.0159±0.0013	0.243±0.007	0.0345±0.0008	5.74±0.63
HD37674	6	0.0412±0.0057	0.145±0.014	0.0300±0.0026	4.55±1.50
HD249845	19	0.0691±0.0239	0.923±0.057	0.0294±0.0017	3.60±0.65
HD249845	43*	0.0127±0.0010	1.210±0.015	0.0321±0.0005	2.86±0.08
HD249845	44*	0.0111±0.0009	1.020±0.012	0.0317±0.0005	2.97±0.09
HD249845	45*	0.0143±0.0009	1.300±0.014	0.0338±0.0005	2.85±0.07
HD249845	71*	0.0129±0.0010	0.972±0.014	0.0268±0.0005	2.87±0.09
HD249845	72*	0.0107±0.0009	0.920±0.012	0.0266±0.0005	2.49±0.07
HD249845	73*	0.0120±0.0009	0.879±0.012	0.0249±0.0004	2.86±0.09
HD252214	6	0.0189±0.0029	0.239±0.013	0.0757±0.0057	2.03±0.22
HD252214	33	0.0128±0.0006	0.247±0.007	0.0852±0.0031	2.62±0.15
HD252214	43*	0.0066±0.0001	0.117±0.002	0.0614±0.0011	3.80±0.18
HD252214	44*	0.0067±0.0001	0.102±0.002	0.0564±0.0010	3.94±0.19
HD252214	71*	0.0069±0.0001	0.119±0.002	0.0582±0.0011	3.24±0.13
HD252214	72*	0.0065±0.0001	0.123±0.002	0.0588±0.0011	3.43±0.15
HD254042	71	0.0116±0.0005	0.399±0.006	0.0396±0.0008	2.39±0.07
HD254042	72	0.0094±0.0005	0.378±0.005	0.0352±0.0006	2.76±0.09
HD259865	6	0.0243±0.0033	0.204±0.013	0.0544±0.0039	2.92±0.46
HD259865	33	0.0139±0.0008	0.205±0.007	0.0660±0.0034	2.24±0.16
HD46994	6*	0.0212±0.0010	0.967±0.012	0.0275±0.0004	3.77±0.14
HD46994	7*	0.0117±0.0010	0.999±0.011	0.0278±0.0003	4.08±0.15
HD46994	33*	0.0076±0.0007	0.563±0.008	0.0232±0.0004	3.15±0.12
HD46883	6	0.0185±0.0059	0.405±0.021	0.0489±0.0026	3.91±0.62
HD46883	33	0.0263±0.0020	0.879±0.018	0.0590±0.0016	2.32±0.09
HD47360	6	0.3619±0.0256	3.231±0.256	0.1111±0.0112	2.06±0.23
HD47360	33	0.0547±0.0050	3.007±0.110	0.1290±0.0066	1.89±0.08
HD52463	6	0.0174±0.0070	0.165±0.020	0.0590±0.0096	1.40±0.29
HD52463	7	-0.0115±0.0171	0.185±0.034	0.0410±0.0079	1.09±0.31
HD52463	33	0.0112±0.0007	0.106±0.005	0.0588±0.0047	1.63±0.13
HD52463	34	0.0147±0.0006	0.086±0.004	0.0431±0.0027	2.35±0.23
HD53755	7	0.0353±0.0052	0.317±0.014	0.0341±0.0014	5.05±0.84
HD53755	33*	0.0053±0.0003	0.436±0.004	0.0342±0.0004	2.98±0.07
HD56876	7*	0.0036±0.0001	0.070±0.001	0.0356±0.0009	2.77±0.12
HD56876	33*	0.0030±0.0001	0.061±0.001	0.0294±0.0006	3.36±0.16
HD56876	34*	0.0036±0.0001	0.063±0.001	0.0307±0.0006	3.43±0.16
HD56876	61*	0.0033±0.0001	0.074±0.001	0.0317±0.0006	3.08±0.12
ALS864	7	0.0278±0.0009	0.084±0.006	0.1351±0.0119	3.36±0.70
ALS864	8	0.0381±0.0017	0.169±0.010	0.1521±0.0030	37.5±23.9
ALS864	34	0.0297±0.0007	0.232±0.037	0.6118±0.1861	1.13±0.11
ALS864	61	0.0276±0.0003	0.269±0.044	0.4931±0.1317	1.22±0.10
HD67536	1	0.1040±0.0094	0.657±0.027	0.0353±0.0010	9.09±1.90
HD67536	4*	0.0163±0.0006	0.703±0.009	0.0324±0.0005	3.28±0.11
HD67536	7*	0.0108±0.0006	0.752±0.010	0.0345±0.0006	2.43±0.06
HD67536	8*	0.0161±0.0007	0.869±0.010	0.0322±0.0004	3.60±0.12
HD67536	9*	0.0119±0.0006	0.849±0.010	0.0334±0.0005	3.10±0.09
HD67536	10*	0.0115±0.0006	0.710±0.009	0.0322±0.0005	3.09±0.10
HD67536	11	0.1552±0.0113	0.629±0.033	0.0330±0.0013	5.79±1.14
HD67536	28*	0.0094±0.0006	1.016±0.010	0.0332±0.0003	3.69±0.10
HD67536	31*	0.0116±0.0006	0.772±0.008	0.0300±0.0004	3.20±0.09
HD67536	34*	0.0121±0.0005	0.767±0.008	0.0335±0.0004	3.60±0.10
HD67536	35*	0.0066±0.0006	0.855±0.011	0.0377±0.0007	2.29±0.05
HD67536	37*	0.0060±0.0006	0.858±0.011	0.0397±0.0007	2.32±0.06
HD67536	38*	0.0112±0.0005	0.641±0.007	0.0306±0.0004	2.98±0.08
HD67536	61*	0.0102±0.0006	0.630±0.009	0.0322±0.0005	2.97±0.10
HD67536	62*	0.0112±0.0006	1.020±0.009	0.0314±0.0003	2.88±0.06
HD67536	63*	0.0189±0.0005	0.612±0.007	0.0299±0.0004	3.94±0.14
HD67536	64*	0.0129±0.0005	0.598±0.007	0.0323±0.0005	3.25±0.10
HD67536	68*	0.0079±0.0006	0.676±0.008	0.0324±0.0005	2.91±0.09
HD67536	69*	0.0120±0.0006	0.712±0.009	0.0313±0.0005	2.79±0.08

Table B.1. Continued

Name	Sector	$C(\text{mmag})$	$A_0(\text{mmag})$	$\tau(\text{d})$	γ
HD68217	7*	0.0051±0.0002	0.879±0.015	0.2007±0.0053	1.73±0.03
HD68217	8*	0.0046±0.0003	0.984±0.013	0.1422±0.0027	2.01±0.04
HD68217	34*	0.0131±0.0003	1.032±0.021	0.1486±0.0046	1.57±0.03
HD68217	35*	0.0105±0.0004	1.096±0.028	0.1153±0.0046	1.47±0.03
HD68217	61*	0.0054±0.0003	0.800±0.014	0.1346±0.0037	1.60±0.03
HD68217	62*	0.0030±0.0002	0.738±0.013	0.1662±0.0046	1.72±0.03
HD68324	7*	0.0032±0.0004	0.453±0.010	0.0808±0.0036	1.35±0.03
HD68324	8*	0.0053±0.0005	0.501±0.013	0.0934±0.0051	1.24±0.03
HD68324	9*	0.0013±0.0004	0.451±0.011	0.0876±0.0045	1.19±0.03
HD68324	34*	0.0022±0.0003	0.701±0.015	0.1520±0.0067	1.15±0.02
HD68324	35*	0.0001±0.0005	0.577±0.014	0.0976±0.0050	1.16±0.03
HD68324	61*	0.0035±0.0004	0.519±0.011	0.1024±0.0046	1.22±0.03
HD68324	62*	0.0024±0.0003	0.439±0.009	0.0779±0.0033	1.29±0.03
HD68962	7*	0.0065±0.0004	0.214±0.004	0.0220±0.0007	2.16±0.08
HD68962	8*	0.0094±0.0004	0.235±0.005	0.0215±0.0006	2.38±0.10
HD68962	34*	0.0066±0.0003	0.188±0.003	0.0186±0.0004	2.92±0.12
HD68962	35*	0.0060±0.0004	0.224±0.004	0.0190±0.0004	2.65±0.10
HD68962	61*	0.0067±0.0003	0.228±0.003	0.0198±0.0003	3.14±0.11
HD75869	8	0.0151±0.0057	0.400±0.033	0.0911±0.0100	2.26±0.37
HD75869	35	0.0073±0.0012	0.342±0.013	0.0909±0.0058	1.77±0.11
HD75869	62	0.0062±0.0002	0.282±0.005	0.0835±0.0021	2.10±0.06
HD78548	8	0.0064±0.0034	0.233±0.013	0.0651±0.0049	2.05±0.24
HD78548	10	0.0051±0.0032	0.223±0.013	0.0690±0.0054	1.99±0.23
HD78548	35*	0.0030±0.0002	0.265±0.004	0.0663±0.0015	1.87±0.04
HD78548	37*	0.0026±0.0001	0.198±0.002	0.0516±0.0009	2.31±0.06
HD78548	62*	0.0026±0.0001	0.205±0.003	0.0812±0.0016	2.19±0.05
HD78548	63*	0.0028±0.0001	0.166±0.002	0.0656±0.0012	2.60±0.07
HD81347	9	0.0091±0.0013	0.111±0.007	0.0774±0.0046	4.22±0.80
HD81347	35	0.0058±0.0005	0.169±0.005	0.0880±0.0028	3.37±0.24
HD81347	36	0.0054±0.0004	0.149±0.004	0.0935±0.0032	3.13±0.22
HD81347	62	0.0033±0.0001	0.124±0.002	0.0823±0.0014	3.82±0.18
HD81347	63	0.0050±0.0001	0.089±0.002	0.0734±0.0018	3.55±0.21
HD87015	21*	0.0066±0.0002	0.249±0.003	0.0423±0.0008	2.38±0.06
HD87015	45*	0.0035±0.0001	0.140±0.002	0.0332±0.0004	5.24±0.24
HD87015	46*	0.0042±0.0001	0.136±0.001	0.0374±0.0002	20.6±1.94
HD87015	48*	0.0056±0.0001	0.157±0.002	0.0377±0.0002	19.0±1.58
HD87015	72*	0.0036±0.0002	0.161±0.002	0.0336±0.0004	4.20±0.17
HD87152	9	0.0121±0.0069	0.470±0.039	0.1053±0.0132	1.66±0.23
HD87152	10	0.0264±0.0062	0.483±0.035	0.0911±0.0089	2.13±0.30
HD87152	36*	0.0072±0.0003	0.668±0.008	0.0934±0.0018	2.10±0.04
HD87152	37*	0.0041±0.0003	0.636±0.009	0.0983±0.0021	2.12±0.05
HD87152	63*	0.0092±0.0003	0.803±0.013	0.1454±0.0040	1.64±0.03
HD93501	10	0.0971±0.0178	2.714±0.104	0.0875±0.0038	3.28±0.32
HD93501	11	0.1508±0.0152	1.625±0.058	0.0744±0.0007	63.4±33.7
HD93501	36	0.0734±0.0048	1.812±0.031	0.0716±0.0005	23.9±3.80
HD93501	37	0.0665±0.0056	1.770±0.051	0.0634±0.0022	3.00±0.20
HD93501	63	0.0183±0.0014	1.371±0.028	0.0808±0.0025	2.03±0.07
HD93501	64	0.0339±0.0017	1.817±0.029	0.0603±0.0015	2.09±0.06
HD97499	10	0.0317±0.0022	0.335±0.012	0.1127±0.0031	7.43±1.25
HD97499	11	0.0232±0.0020	0.264±0.012	0.1030±0.0051	3.51±0.45
HD97499	37	0.0148±0.0008	0.308±0.008	0.1034±0.0030	3.73±0.28
HD97499	64	0.0122±0.0002	0.249±0.004	0.1015±0.0016	3.83±0.16
HD97913	10	0.0340±0.0083	0.496±0.028	0.0483±0.0031	2.78±0.39
HD97913	11	0.0195±0.0108	0.640±0.042	0.0698±0.0064	1.78±0.22
HD97913	37	0.0191±0.0020	0.476±0.014	0.0481±0.0019	2.65±0.18
HD97913	64*	0.0104±0.0003	0.491±0.005	0.0391±0.0005	2.97±0.07
HD108257	10*	0.0045±0.0001	0.082±0.001	0.0257±0.0004	4.64±0.26
HD108257	11*	0.0047±0.0001	0.096±0.001	0.0230±0.0004	4.33±0.23
HD108257	37*	0.0036±0.0001	0.077±0.001	0.0243±0.0002	8.97±0.64
HD125238	11*	0.0024±0.0002	0.313±0.005	0.0845±0.0020	1.95±0.05
HD125238	38*	0.0015±0.0001	0.220±0.004	0.1010±0.0033	1.51±0.03
HD125238	65*	0.0014±0.0001	0.217±0.003	0.0779±0.0018	2.09±0.05
HD133385	12	0.0138±0.0040	0.317±0.016	0.0654±0.0043	2.18±0.23
HD133385	38	0.0043±0.0010	0.384±0.009	0.0700±0.0026	2.12±0.10
HD133385	39	0.0063±0.0009	0.350±0.007	0.0621±0.0017	2.58±0.12
HD133385	65	0.0054±0.0003	0.357±0.005	0.0609±0.0012	2.35±0.06
HD133385	66	0.0061±0.0003	0.419±0.005	0.0665±0.0012	2.46±0.06
HD136298	11*	0.0087±0.0003	0.377±0.008	0.0802±0.0028	1.64±0.04
HD136298	38*	0.0025±0.0002	0.370±0.006	0.1184±0.0040	1.31±0.02
HD136298	65*	0.0009±0.0002	0.328±0.007	0.1125±0.0046	1.24±0.02
HD138485	Kep.	0.0302±0.0008	0.035±0.003	0.0487±0.0039	3.72±0.86
HD142378	Kep.	0.0643±0.0534	0.203±0.187	0.2062±0.4356	0.53±0.55
HD143118	12*	0.0028±0.0002	0.549±0.014	0.3872±0.0203	1.12±0.02
HD143118	65*	0.0013±0.0002	0.459±0.008	0.1605±0.0056	1.25±0.02
CPD-50 9216	12	0.1145±0.0193	1.146±0.111	0.0829±0.0112	1.63±0.23
CPD-50 9216	39	0.0368±0.0027	0.694±0.020	0.0472±0.0016	3.11±0.22
CPD-50 9216	66	0.0298±0.0009	1.013±0.018	0.0557±0.0015	2.04±0.06
CPD-48 8710	12	0.0670±0.0054	0.379±0.047	0.1759±0.0364	1.46±0.24
CPD-48 8710	39	0.0228±0.0017	0.569±0.032	0.1484±0.0143	1.41±0.08
CPD-48 8710	66	0.0227±0.0004	0.501±0.012	0.0859±0.0029	1.94±0.06
HD150745	12*	0.0074±0.0002	0.390±0.005	0.1073±0.0020	2.23±0.05
HD150745	39*	0.0036±0.0001	0.274±0.003	0.0915±0.0016	2.13±0.04
HD150745	66*	0.0028±0.0002	0.468±0.006	0.1434±0.0034	1.70±0.03

Table B.1. Continued

Name	Sector	C(mmag)	A_0 (mmag)	τ (d)	γ
HD164900	40*	0.0061±0.0003	0.433±0.005	0.0744±0.0008	4.69±0.19
HD164900	53*	0.0053±0.0003	0.724±0.005	0.0748±0.0004	7.66±0.27
HD166197	13	0.0004±0.0034	0.306±0.027	0.2312±0.0408	1.07±0.11
HD166197	66*	0.0030±0.0001	0.164±0.002	0.0568±0.0007	3.16±0.09
HD168905	13*	0.0029±0.0001	0.085±0.001	0.0402±0.0007	3.06±0.11
HD168905	66*	0.0027±0.0001	0.150±0.002	0.0509±0.0010	2.34±0.07
HD180968	14*	0.0123±0.0006	1.442±0.021	0.1202±0.0031	1.58±0.03
HD180968	40*	0.0177±0.0006	1.093±0.012	0.0574±0.0008	2.94±0.08
HD180968	54*	0.0053±0.0008	1.374±0.024	0.0855±0.0026	1.60±0.03
HD192968	14	0.0127±0.0034	0.315±0.056	0.5142±0.1992	0.94±0.14
HD192968	15	0.0198±0.0024	13.21±176.7	216.06±3678.3	0.84±0.15
HD192968	41*	0.0052±0.0001	0.138±0.004	0.0944±0.0049	1.38±0.04
HD192968	55*	0.0060±0.0001	0.012±0.001	0.0098±0.0004	5.16±0.77
Cl* Berkeley 86 HG 261	14	0.0395±0.0046	0.729±0.077	0.3663±0.0713	1.19±0.11
Cl* Berkeley 86 HG 261	15	0.0806±0.0030	0.411±0.036	0.2415±0.0301	2.03±0.28
Cl* Berkeley 86 HG 261	41	0.0314±0.0007	0.480±0.029	0.4920±0.0545	1.38±0.08
Cl* Berkeley 86 HG 261	55	0.0358±0.0010	0.437±0.030	0.3809±0.0500	1.24±0.08
HD193794	14	0.0265±0.0069	0.759±0.032	0.0747±0.0042	2.23±0.20
HD193794	15	0.0393±0.0061	0.649±0.026	0.0623±0.0029	2.88±0.29
HD193794	41*	0.0070±0.0003	0.716±0.006	0.0595±0.0007	2.52±0.05
HD193794	55*	0.0071±0.0003	0.584±0.005	0.0519±0.0006	2.69±0.05
HD198781	15*	0.0118±0.0005	0.733±0.008	0.0452±0.0005	3.58±0.11
HD198781	17*	0.0131±0.0005	0.642±0.007	0.0437±0.0005	3.90±0.13
HD198781	18*	0.0108±0.0004	0.625±0.007	0.0443±0.0006	3.59±0.11
HD198781	24*	0.0110±0.0004	0.624±0.006	0.0457±0.0005	4.04±0.12
HD198781	56*	0.0042±0.0004	0.554±0.005	0.0428±0.0005	3.82±0.11
HD198781	57*	0.0056±0.0004	0.642±0.007	0.0439±0.0005	3.42±0.10
HD198781	58*	0.0044±0.0004	0.592±0.006	0.0480±0.0007	2.79±0.07
HD201819	15*	0.0094±0.0003	0.419±0.004	0.0325±0.0003	3.87±0.11
HD201819	55*	0.0045±0.0003	0.436±0.004	0.0378±0.0005	2.77±0.06
HD201819	56*	0.0032±0.0002	0.373±0.003	0.0358±0.0004	2.93±0.06
HD207308	16	-0.0004±0.0069	0.219±0.014	0.0304±0.0020	2.23±0.32
HD207308	17	-0.0091±0.0107	0.245±0.021	0.0346±0.0031	1.64±0.27
HD207308	24	0.0036±0.0045	0.184±0.009	0.0282±0.0014	2.81±0.36
HD207308	56	0.0048±0.0002	0.152±0.002	0.0311±0.0007	2.27±0.07
HD207308	57	0.0042±0.0003	0.185±0.003	0.0342±0.0009	2.11±0.07
HD207308	58	0.0037±0.0002	0.167±0.003	0.0331±0.0008	2.10±0.06
LS III +57 89	16	0.0394±0.0023	0.413±0.052	0.5356±0.1214	1.33±0.16
LS III +57 89	17	0.0433±0.0018	0.429±0.027	0.2379±0.0181	2.41±0.24
HD216092	16	0.0152±0.0150	0.341±0.029	0.0280±0.0023	2.39±0.46
HD216092	17	0.0093±0.0258	0.465±0.051	0.0311±0.0032	1.75±0.36
HD216092	56	0.0076±0.0006	0.460±0.007	0.0374±0.0010	1.96±0.05
HD216092	57	0.0120±0.0006	0.481±0.007	0.0316±0.0007	2.32±0.07
NGC 7654 485	17	0.0679±0.0050	0.606±0.057	0.2505±0.0403	1.45±0.17
NGC 7654 485	18	0.0603±0.0046	0.606±0.060	0.2399±0.0377	1.61±0.20
NGC 7654 485	24	0.0352±0.0025	0.251±0.022	0.1780±0.0219	2.28±0.39
NGC 7654 485	57	0.0434±0.0004	0.341±0.011	0.1715±0.0083	2.28±0.14
NGC 7654 485	58	0.0577±0.0005	0.626±0.033	0.2598±0.0194	1.80±0.10
HD223145	1*	0.0051±0.0001	0.295±0.002	0.1008±0.0010	4.01±0.11
HD223145	2*	0.0045±0.0001	0.268±0.002	0.0955±0.0004	12.5±0.61
HD223145	28*	0.0035±0.0001	0.330±0.004	0.0942±0.0013	3.33±0.09
HD223145	29*	0.0058±0.0001	0.302±0.003	0.0922±0.0012	3.46±0.10
HD223145	68*	0.0038±0.0001	0.309±0.004	0.0824±0.0017	2.10±0.05
HD223145	69*	0.0032±0.0001	0.329±0.005	0.0927±0.0024	1.77±0.04

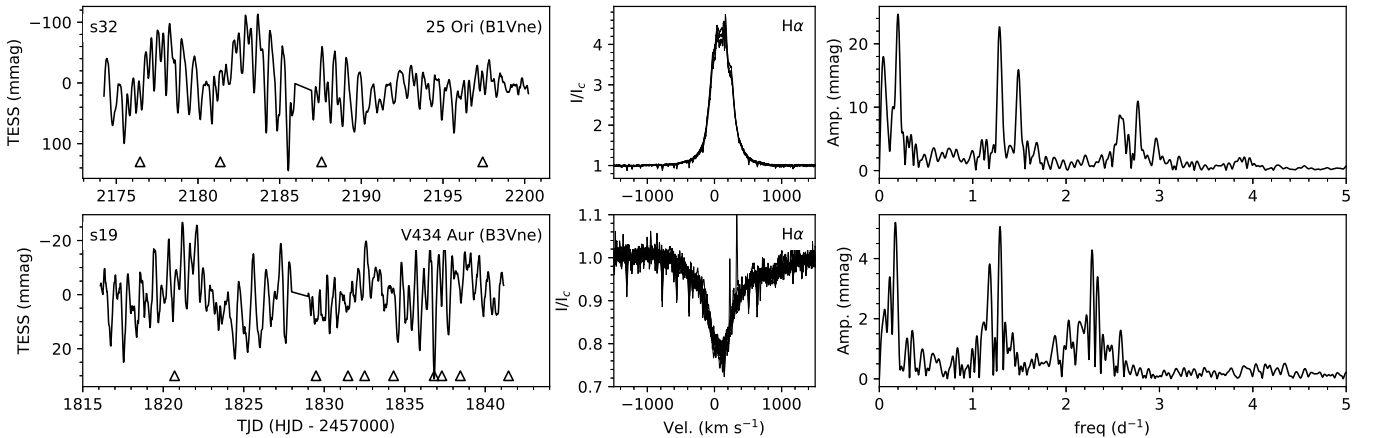


Fig. D.1. TESS photometry and contemporaneous spectroscopy for two Be stars, 25 Ori (top) and V434 Aur (bottom). The left panels show the TESS light curve from the indicated sector (at the top left), with triangles corresponding to dates of NRES spectroscopic observations. The middle panels show the spectral region centred on H α for each spectroscopic epoch shown in the left panels. The right panels contain the frequency spectra built from the TESS photometry.

Table C.1. Properties of isolated signals detected in our sample.

Name	Low Frequencies (0.5–6.0 d ⁻¹) in d ⁻¹ (amplitudes in mmag)		High frequencies (6.–15. d ⁻¹)	Very high frequencies (> 15 d ⁻¹)
	dominant peak	other prominent peaks	frequencies in d ⁻¹ (amplitudes in mmag)	frequencies in d ⁻¹ (amplitudes in mmag)
HD5882	2.540 (2.5–2.9)	4.86 (0.3–0.5)	9.874 (0.2–0.6), 14.63 (0.1)	
NGC 869 133				15.060 (0.3–0.5)
BD+56 538	5.516 (0.8–0.9)	0.960 (1.9) in Sector 58	7.452 (0.2) in Sector 58	
HD14250	0.812 (24.3–25.5)			
BD+62 657		5.034 (0.2)	8.692 (0.3–0.4), 9.152 (0.2), 9.692 (0.2), 12.984 (0.1–0.2), 14.520 (0.5–0.6)	26.572(0.12) in Sector 59
HD34748			7.618 (0.2–0.3), 9.310 (0.1–0.2)	
HD35532	1.764 (2.1–4.0) + 3.524 (1.9–4.7)	3.090 (1.2–1.5) except Sector 43		
HD35777	1.716 (2.5) + 3.428 (2.5)		6.856 (0.2), 8.132 (0.2), 9.888 (0.2), 12.000 (0.09) ^{a1}	18.128 (0.05) ^{a2}
HD37303	2.140 (0.35)	1.620 (0.1), 1.870 (0.2), 4.252 (0.1)	11.788 (0.3), 13.430 (0.2), 14.980 (0.07)	19.292(0.3), 23.632(0.05) ^b
HD37397	1.744 (9.0)	3.492 (5.4)	6.982 (0.5), 10.468 (0.2), 12.210 (0.2)	15.708 (0.13)
HD37674	2.764 (5.8)	3.304 (1.1)	6.076 (2.1), 6.612 (0.6), 12.144 (0.4), 12.664 (0.5)	
HD252214	1.456 (1.6–1.9)	0.728 (0.7–1.0), 2.904 (0.2–0.3), 3.032 (0.2–0.3)		
HD254042		4.990 (0.8–1.0)		
HD259865		0.582 (1.0–1.4)	7.640 (0.1–0.2)	
HD46883	1.764 (1.7–2.3) + 2.660 (1.4–1.5)			
HD52463		2.354(0.4) + 3.286 (0.3–0.4) in Sectors 6–7		
HD53755	1.536 (4.5–5.9) + 3.388 (5.1–5.9)	2.86 (1.4–1.8), 3.76 (1.1–3.1)		
HD56876	1.724 (1.1)	3.448 (0.3), 4.552 (0.3–0.4)	6.288 (0.2), 8.806 (0.17)	22.400 (0.02), 24.124 (0.02–0.03)
ALS 864	0.835 (0.4–0.5)			
HD68324			8.778 (1.5–2), 10.704 (3.0–3.3)	
HD87015	3.532 (2.7–3.1)	1.970 (0.6–1.2)		
HD87152	1.086 (2.2–5.5) + 1.290 (1.9–3.9)	2.536 (1.2–1.8)		37.184 (0.02–0.05)
HD97499	1.046 (1.8–2.0)	0.750 (1.4–1.7), 3.010 (0.2–0.3)		
HD97913	2.176 (4.0–5.9)	5.534 (1.4–1.9)	11.072 (0.2) in Sector 64	
HD108257				28.120 (0.03) in Sector 10
HD133385	1.080 (1.1–3.8)	2.000 (1.0–1.5)		
HD136298	5.900 (1.2–1.4)	1.276 (0.9–1.6), 2.538 (0.6–0.8), 2.700 (0.4–0.5), ^c	8.096 (0.2–0.3), 8.580 (0.02), 9.300 (0.2), 9.770 (0.1–0.2), 10.576 (0.1–0.2), 11.746 (0.2)	
HD138485	1.943 (1.7)	0.560 (0.7), 1.607 (0.4), 1.655 (0.4), ^d	6.155 (0.2), 11.401 (0.15)	
HD142378		1.451 (1.0), 1.730 (0.9), 3.865 (1.3)		
HD143118			6.060 (0.2–0.3), 6.566 (0.2–0.3) ^{e1}	26.234 (0.03–0.04) ^{e2}
CPD–50 9216		1.536 (3.6–3.9)		
CPD–48 8710	1.688 (2.4–2.6)	3.376 (0.9–1), 5.060 (0.4–0.5)	6.752 (0.4–0.6)	18.396 (0.3)
HD150745		0.938 (1.1–1.4)		
HD164900	0.65 (3.5–4.1) + 1.406 (3.4–5.2)	1.842 (2.2–2.6), 4.610 (0.3)		
HD168905		1.184 (0.8) in Sector 66	11.896(0.2) in Sector 66	
HD180968	0.640 (7.6–9.5)	3.246 (1.6–2.8)		
HD192968		5.964 (0.08–0.1) ^{f1}	9.392 (0.2–0.4), 10.012 (0.2–0.9), 13.504 (0.11–0.13)	20.364 (0.07–0.13), 20.604 (0.13), ^{f2}
Cl* Berk. 86 HG 261		5.926 (0.3–0.4)	6.926 (0.3), 13.282 (0.2)	
HD198781	1.536 (5.3–7.0)	2.554 (4.2–5), 2.914 (1.9–2.2)		
HD201819	^g			
HD207308	2.822 (0.8–1.5) + 4.510 (0.8–1.0)	4.304 (0.7–0.9) in Sectors 16 and 17	6.86 (0.8–1.), 9.118 (0.2, except Sect. 16, 17)	
HD223145		5.010 (0.1–0.5)		

Notes. ^{a1} plus 13.716(0.06) in Sector 32; ^{a2} plus 15.432 (0.06), 20.576 (0.02), 25.716 (0.02), and 29.148 (0.02) in Sector 32; ^b plus 26.308 (0.05) and 34.272 (0.07) in Sector 6, and 24.896 (0.05) in Sector 32; ^c 4.710 (0.03), 4.870 (0.02); ^d 1.851 (0.4), 2.076 (0.8), 2.561 (0.5), 3.550 (0.4), 3.685 (0.8), 5.630 (0.3); ^{e1} plus 9.740 (0.15) in Sector 12 and 6.728 (0.2) in Sector 12; ^{e2} not formally significant but coherent between sectors; ^{f1} plus 1.628 (0.5) and 1.868 (0.4) in Sector 41; ^{f2} 29.314 (0.07), 29.632 (0.03–0.06), 33.966 (0.03), 36.074 (0.05), 37.200 (0.03–0.04), 40.190 (0.03–0.05), 40.726 (0.03) plus 32.396 (0.07) in Sector 41 and 35.376 (0.03) in Sector 55; ^g 1.448 (3.4) in Sector 15, 2.766 (1.7–1.9) in Sectors 55 and 56.

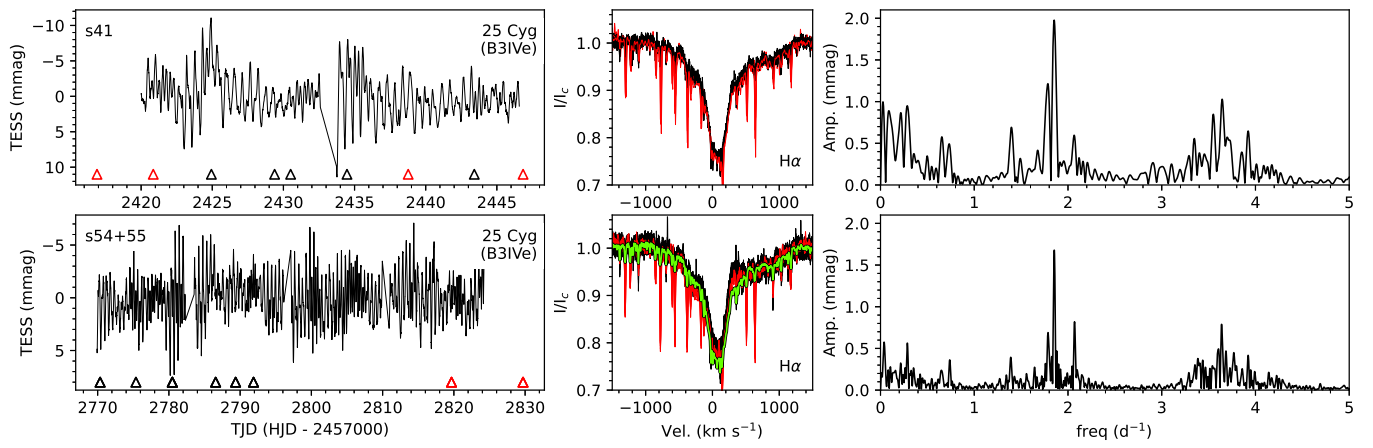


Fig. D.2. Similar to Fig. D.1, but comparing two epochs for the same Be star (25 Cyg). The black (respectively red) triangles in the left panels indicate spectra from NRES (respectively DAO). The same colours are used in the middle panels for data from the two telescopes. The green line in the bottom-middle panel is the average of the NRES $H\alpha$ profile taken during Sector 41 (i.e. during an emission-free phase).